

CHALMERS



Peyman Jafarian

Numerical Simulation of the Flow Around a Multi-Element Airfoil

Department of Applied Mechanics
Division of Fluid Dynamics
CHALMERS UNIVERSITY OF TECHNOLOGY
Göteborg Sweden, 2010

Master's Thesis [2010 : 46]

MASTER'S THESIS 2010:46

**Numerical Simulation of the Flow Around a
Multi-Element Airfoil**

Master's Thesis

PEYMAN JAFARIAN

Department of Applied Mechanics
Division of Fluid Dynamics
CHALMERS UNIVERSITY OF TECHNOLOGY
Göteborg, Sweden, 2010

Numerical Simulation of the Flow Around a Multi-Element Airfoil

Master's Thesis

Peyman Jafarian

© PEYMAN JAFARIAN, 2010

Master's Thesis 2010:46

ISSN: 1652-8557

Department of Applied Mechanics,

Division of Fluid Dynamics

Chalmers University of Technology

SE-412 96 Göteborg, Sweden

Phone +46-(0)31-7721400

Fax: +46-(0)31-180976

Printed at Chalmers Reproservice

Göteborg, Sweden 2010

Numerical Simulation of the Flow Around a Multi-Element Airfoil

Master's Thesis

by

Peyman Jafarian

jafarian@student.chalmers.se

Department of Applied Mechanics

Division of Fluid Dynamics

Chalmers University of Technology

Abstract

Numerical calculations were carried out on the high-lift three-element airfoil at the freestream Mach number of $M_\infty = 0.15$. The flow around three-element airfoil was computed using an explicit algebraic Reynolds stress (EARSM) formulation coupled with the standard $k - \omega$ model, which was applied to high lift configuration. Moreover, Spalart-Allmaras (S-A), PDH LRN $k - \omega$ model, and Menter SST $k - \omega$ models were used to investigate the ability of turbulence models in predicting the complex flow-field. Four different angles of attack at $\alpha = 6^\circ$, $\alpha = 6.75^\circ$, $\alpha = 7.05^\circ$ and $\alpha = 7.5^\circ$ were examined to correct the angle of attack for numerical computations in order to get the best agreement with wind-tunnel experimental data.

The computations were compared with experimental data and the ability of the models to predict the flow-field phenomena such as flow separation induced by adverse pressure gradient was examined. In steady two-dimension simulation, the S-A and PDH LRN $k - \omega$ turbulence models showed better behavior compared with the Hellsten $k - \omega$ and Menter SST $k - \omega$ models, whereas the other models under-predict the pressure distribution on the suction side of the airfoil. The ability of models to predict the trailing edge separation was investigate and the results obtained respectively with the S-A model and the PDH LRN $k - \omega$ models were in good agreement with experimental data, but other models have predicted an early separation on the flap. At the end of the project a laminar area was prescribed on the leading edge of each element and the flow was computed with local transition prescribed. The Menter SST model produced poor results and the flow is completely separated over the flap. Other models predict higher peak pressure on the suction side of the airfoil (higher lift force) and the results with this assumption were more consistent with experimental data.

Keywords: Multi-element airfoil, turbulent flow, turbulence models, flow separation, local transition, CFD Edge solver

Acknowledgement

I would like to express my sincere gratitude to my supervisors, Professor Shia-Hui Peng and Professor Lars Davidson. I would like to thank them specially for their trust and patience during the first months. Their comments helped me doing the thesis and this thesis would never have reached this point without their enlightening discussions and brilliant advice. Also I would like to thank them for their great support, encouragement and guidance during this work.

This thesis has been done with EDGE software, thanks to Swedish Defense Research Agency, FOI, and also Peter Eliasson for providing the support during the thesis work.

This thesis have performed in the framework of EC ATAAC project. I also want to acknowledge the German Aerospace Center (DLR), for providing the experimental data which was very useful and worthwhile for this work.

I have to say thanks to Ilyas and Giovanni whom I learned a lot from. They always had time for my questions. And, of course, all the people at the Department for their help and support They are all kind and helpful.

It is only due to my family that I am here. Expressing my feeling is impossible and I can just say thanks to them.

Nomenclature

Upper-case Roman

C_l	Lift force coefficient
C_d	Drag force coefficient
C_m	Pitching moment coefficient
C_f	Skin friction coefficient
C_p	Pressure coefficient
F_d	Drag force
F_l	Lift force
M	Mach number
T	Temperature
R	Gas constant
U	Streamwise mean velocity

Lower-case Roman

n	Normal direction
c	Chord length
p	Pressure
x	Streamwise direction
k	Turbulence kinetic energy
q	Velocity

Upper-case Greek

Ω	Vorticity
----------	-----------

Lower-case Greek

τ_w	Wall shear stress
μ	Dynamic viscosity
ν	Kinematic viscosity
ρ	Density
μ_t	Turbulence dynamic viscosity
ν_t	Turbulence kinematic viscosity

Abbreviations

S-A	Spalart-Allmaras
ZPG	Zero Pressure Gradient
RANS	Reynolds Average Navier-Stokes
Re	Reynolds number
DNS	Direct Numerical Simulation
EARSM	Explicit Algebraic Reynolds Stress Model
AoA	Angle of Attack

subscripts

∞	Freestream
----------	------------

Contents

Abstract	v
Acknowledgement	vii
Nomenclature	viii
1 Theory	1
1.1 Turbulence models	1
1.1.1 EARSM + Hellsten k - ω model	1
1.1.2 Menter SST k - ω model	3
1.1.3 Spalart-Allmaras one-equation model (S-A)	4
1.1.4 Peng-Davidson-Holmberg (PDH) LRN k - ω model	5
2 Method	7
2.1 Criteria for comparison of turbulence models	7
2.2 Case setup	8
2.2.1 General information about the EDGE	8
2.2.2 Mesh information and setup procedure	9
2.3 Description of analyzed variables	11
2.3.1 Pressure Coefficient	11
2.3.2 Friction coefficient and separation phenomena	12
2.3.3 Pitching moment coefficient	13
2.3.4 Prescribed local transition	13
3 Numerical Results and discussion	15
3.1 Results at angle of attack, $\alpha = 7.05^\circ$	15
3.2 Effect of changing the angle of attack	26
3.3 Computation with Local prescribed transition	33
3.4 Comparing velocity field	43
3.5 Comparing turbulent viscosity	46
4 Summary and Conclusion	49

Chapter 1

Theory

1.1 Turbulence models

Turbulence models based on the RANS approach are used for analyzing and simulating the flow-field around the high-lift multi-element airfoil. These models are: the EARSM + Hellsten k - ω model, the Spalart-Allmaras model, the Menter SST k - ω model and the Peng-Davidson-Holmberg (PDH) LRN k - ω model.

In this part four RANS turbulence models which are used for steady two dimensional simulations are explained and some details and advancements of these models will be reviewed.

1.1.1 EARSM + Hellsten k - ω model

Turbulence models which are used in aerodynamic applications are usually developed based on the two transport equations for calculating turbulence scales. The Reynolds stress tensor is modeled based on the Boussinesq assumption which relates the turbulent stresses to the mean strain rate tensor. This relation is usually linear in many eddy-viscosity based models and may become awkward in modeling of complex flow. Flow around the multi-element airfoil is usually characterized by boundary layer transition, confluence of boundary layer, boundary layer separation and trailing wakes [1]. In such cases advanced turbulence models are needed for reliable predictions of the flow field. Reynolds-stress model (RSM) covers a wider range of applications because modeled transport equation is solved for each stress, but it is rather complicated for industrial aerodynamic designs. However, it is possible to extend the application of two-equation models by using more advanced nonlinear equation for modeling the Reynolds stress. Explicit Algebraic Reynolds stress Model (EARSM) is a suitable nonlinear constitutive

model which can be used with two-equation models.

The Hellsten $k-\omega$ model is designed for aerodynamic problems especially for high-lift aerodynamics and concentrate on the boundary layer under adverse pressure gradient, wake and mixing layer which are the dominant phenomena in high-lift aerodynamics [2]. The new model uses (EARSM) as a constitutive equation to make a relation between Reynolds stress and mean-velocity gradient. Moreover, the scale determining model is based on the $k-\omega$ formulation and model equations are similar to Menter's $k-\omega$ model, but the model is recalibrated by focusing on the aerodynamics applications. In order to avoid discrepancies between numerical simulation and experimental data, Hellesten suggested that diffusion coefficient of k needs a stricter limit, namely $\sigma_k > 1$, when EARSM is used as a constitutive model, but when linear constitutive equation is used it is enough to have $\sigma_k > 0.5$. Before calibrating the model, he investigated three main constrains based on the model behavior near edges of shear layers by considering that C_μ coefficient is variable in the nonlinear constitutive modeling. He found the following relations:

$$\begin{aligned}\sigma_w - \sigma_k + \sigma_d &> 0 \\ \sigma_k - \sigma_d &> 0 \\ \sigma_k &> 1\end{aligned}$$

In reference [2], Hellsten mentioned that "the most of the existing $k-\omega$ models do not satisfy equations the above constrains" and this will leads to the unphysical sensitivity to the freestream values. This sensitivity happens when $\sigma_k = \sigma_w$ and $\sigma_d = 0$. Hellsten calibrated the model coefficients based on the different cases like zero-pressure-gradient (ZPG) and adverse pressure gradient, fully developed plane channel flow, plane far wakes and mixing layer.

$$\frac{D\rho k}{Dt} = \tau_{ij} \frac{\partial U_i}{\partial x_j} - \beta^* \rho k \omega + \frac{\partial}{\partial x_k} \left[(\mu + \sigma_k \mu_t) \frac{\partial k}{\partial x_k} \right] \quad (1.1)$$

$$\begin{aligned}\frac{D\rho\omega}{Dt} &= \gamma \frac{\omega}{k} \tau_{ij} \frac{\partial U_i}{\partial x_j} - \beta \rho \omega^2 + \frac{\partial}{\partial x_k} \left[(\mu + \sigma_\omega \mu_t) \frac{\partial \omega}{\partial x_k} \right] \\ &+ \sigma_d \frac{\rho}{\omega} \max \left(\frac{\partial k}{\partial x_k} \frac{\partial \omega}{\partial x_k}; 0 \right)\end{aligned} \quad (1.2)$$

$$\mu_t = (C_\mu / \beta^*) (\rho k / \omega) \quad (1.3)$$

$$\tau_{ij} = \mu_t \left(\frac{\partial U_i}{\partial x_j} + \frac{\partial U_j}{\partial x_i} - \frac{2}{3} \frac{\partial U_k}{\partial x_k} \delta_{ij} \right) - \frac{2}{3} \rho k \delta_{ij} - a_{ij}^{(ex)} \rho k \quad (1.4)$$

More details of equation derivation is explained in reference [2].

1.1.2 Menter SST k - ω model

Menter SST model is an eddy viscosity model which is a combination of $k - \epsilon$ model and $k - \omega$ model. This model is mainly developed to perform better in presence of adverse pressure gradient effect.

The $k - \omega$ model does not involve any damping function and is considered to be superior especially in predicting the flow near the wall. The behavior of the $k - \omega$ model is superior to the $k - \epsilon$ model in viscous sublayer and logarithmic part of boundary layer [3]. However, in the wake region of the boundary layer, the $k - \epsilon$ model is superior in comparison with the $k - \omega$ model because the $k - \omega$ model has a very strong sensitivity to the free stream values specified for ω outside the boundary layer [3].

To achieve the desired features in the different regions, the standard high-Reynolds-number version of the $k - \epsilon$ model will be transformed to a $k - \omega$ formulation. It will then multiplied by a blending function $(1 - F_1)$ and added to the original $k - \omega$ model times F_1 . Below the model equations are presented.

$$\frac{D\rho k}{Dt} = \tau_{ij} \frac{\partial U_i}{\partial x_j} - \beta^* \rho \omega k + \frac{\partial}{\partial x_j} \left[\left(\mu + \sigma_k \mu_t \frac{\partial k}{\partial x_j} \right) \right] \quad (1.5)$$

$$\begin{aligned} \frac{D\rho\omega}{Dt} &= \frac{\gamma}{\nu_t} \tau_{ij} \frac{\partial U_i}{\partial x_j} - \beta \rho \omega^2 + \frac{\partial}{\partial x_j} \left[\left(\mu + \sigma_\omega \mu_t \frac{\partial \omega}{\partial x_j} \right) \right] \\ &+ 2(1 - F_1) \rho \sigma_{\omega 2} \frac{1}{\omega} \frac{\partial k}{\partial x_j} \frac{\partial \omega}{\partial x_j} \end{aligned} \quad (1.6)$$

$$\phi = F_1 \phi_1 + (1 - F_1) \phi_2 \quad (1.7)$$

$$\mu_t = \frac{a_1 \rho k}{\max(a_1 \omega; \Omega F_2)} \quad (1.8)$$

$$\tau_{ij} = \mu_t \left(\frac{\partial U_i}{\partial x_j} + \frac{\partial U_j}{\partial x_i} - \frac{2}{3} \frac{\partial U_k}{\partial x_k} \delta_{ij} \right) - \frac{2}{3} \rho k \delta_{ij} \quad (1.9)$$

More details about this models and closure coefficients are given in reference [3].

1.1.3 Spalart-Allmaras one-equation model (S-A)

The Spalart-Allmaras (S-A) is a one equation turbulence model which is written in term of the eddy viscosity. This model solves one transport equation for a quantity which is equivalent to the eddy viscosity. Since turbulence modeling in the context of RANS approach is characterized by two scales, e.g. velocity and length scales, and the model only solves for one property, additional information is needed. The Spalart-Allmaras model uses the wall distance, that would be active through the complete boundary layer, not only in the viscous sub layer. The model includes eight closure coefficients and three damping functions. The equations are defined as follows:

Kinematic turbulent viscosity

$$\mu_T = \rho \tilde{\nu} f_{v1} \quad (1.10)$$

Eddy viscosity equation

$$\frac{\partial \rho \tilde{\nu}}{\partial t} + U_j \frac{\partial \rho \tilde{\nu}}{\partial x_j} = c_{b1} \rho \tilde{S} \tilde{\nu} - c_{w1} f_w \rho \left(\frac{\tilde{\nu}}{d} \right)^2 + \frac{1}{\sigma} \frac{\partial}{\partial x_k} \left[(\mu + \rho \tilde{\nu}) \frac{\partial \tilde{\nu}}{\partial x_k} \right] + \frac{c_{b2} \rho}{\sigma} \frac{\partial \tilde{\nu}}{\partial x_k} \frac{\partial \tilde{\nu}}{\partial x_k} \quad (1.11)$$

Closure coefficients

$$c_{b1} = 0.1355, \quad c_{b2} = 0.622, \quad c_{v1} = 7.1, \quad \sigma = 2/3$$

$$c_{w1} = \frac{c_{b1}}{\kappa^2} + \frac{(1 + c_{b2})}{\sigma}, \quad c_{w2} = 0.31, \quad c_{w3} = 0.33, \quad \kappa = 0.41$$

Auxiliary Relations

$$f_{v1} = \frac{\chi^3}{\chi^3 + c_{v1}^3}, \quad f_{v2} = 1 - \frac{\chi}{1 + \chi f_{v1}}, \quad f_w = g \left[\frac{1 + c_{w3}^6}{g^6 + c_{w3}^6} \right]^{1/6}$$

$$\chi = \frac{\tilde{\nu}}{\nu}, \quad g = r + c_{w2} (r^6 - r), \quad r = \frac{\tilde{\nu}}{\tilde{S} k^2 d^2}$$

$$\tilde{S} = S + \frac{\tilde{\nu}}{k^2 d^2} f_{v2}, \quad S = \sqrt{2 \Omega_{ij} \Omega_{ij}}$$

$$\Omega_{ij} = \frac{1}{2} \left(\frac{\partial U_i}{\partial x_j} - \frac{\partial U_j}{\partial x_i} \right)$$

More details about this model can be found in reference [4].

1.1.4 Peng-Davidson-Holmberg (PDH) LRN $k-\omega$ model

This model was developed based on the $k - \omega$ formulation which has advantages in comparison with low-Reynolds-number models based on the $k - \epsilon$ formulation. Turbulence models which are developed based on the $k-\epsilon$ formulation have a problem with specifying ϵ at the wall. Moreover, damping functions used in LRN models usually rely on wall proximity variables. LRN $k - \epsilon$ models may produce inaccurate predictions for turbulence recirculating flows, such as for the flow around a multi-element airfoil[5].

The PDH LRN model is an improved form of the LRN $k - \omega$ model. A turbulent cross diffusion term is added to the modeled ω equation, in analogy to its viscous counterpart in the exact transport equation. The model constants are re-established and new damping functions which are dependent on the turbulent Reynolds number R_t are established in order to make the model asymptotically consistent as the wall is approached. The modified model has been calibrated in the channel flow, a backward facing step flow with a large expansion ratio and recirculating flow in a ventilation enclosure [5]. A summary of the model equations are presented in the following:

$$\frac{\partial(\rho U_j k)}{\partial x_j} = \tau_{ij} \frac{\partial U_i}{\partial x_j} - c_k f_k \rho \omega k + \frac{\partial}{\partial x_j} \left[\left(\mu + \frac{\mu_t}{\sigma_k} \right) \frac{\partial k}{\partial x_j} \right] \quad (1.12)$$

$$\begin{aligned} \frac{\partial(\rho U_j \omega)}{\partial x_j} &= c_{\omega 1} f_{\omega} \frac{\omega}{k} \tau_{ij} \frac{\partial U_i}{\partial x_j} - c_{\omega 2} \rho \omega^2 \\ &+ \frac{\partial}{\partial x_j} \left[\left(\mu + \frac{\mu_t}{\sigma_{\omega}} \right) \frac{\partial \omega}{\partial x_j} \right] + C_{\omega} \frac{\mu_t}{k} \left(\frac{\partial k}{\partial x_j} \frac{\partial \omega}{\partial x_j} \right) \end{aligned} \quad (1.13)$$

$$\mu_t = c_{\mu} f_{\mu} \frac{\rho k}{\omega} \quad (1.14)$$

$$\tau_{ij} = \mu_t \left(\frac{\partial U_i}{\partial x_j} + \frac{\partial U_j}{\partial x_i} - \frac{2}{3} \frac{\partial U_k}{\partial x_k} \delta_{ij} \right) - \frac{2}{3} \rho k \delta_{ij} \quad (1.15)$$

More details can be found in reference [5].

Chapter 2

Method

2.1 Criteria for comparison of turbulence models

Before starting to compare the obtained results from different turbulence models, it is important to have a criteria for comparing these models. In the context of steady aerodynamics, four main criterium will be presented in order to have a basis for comparing turbulence models. Aerodynamic flows are usually complex flows which are characterized by high Reynolds number usually at the order of million, different range of Mach numbers from subsonic condition during the landing and takeoff to supersonic case, combination of different flow regimes like laminar and turbulent flow. The flow is usually attached or separated at specific part of airfoil. When the angle of attack is increased large-scale separation or unsteadiness often appear in the flow. To predict the correct behavior of aerodynamic flows, it is needed to compute the boundary layer, laminar-turbulence transitional onset, transitional flow, separation point, separated flow, formation of shock and shock-boundary-layer interaction [6]. In terms of the computational efficiency with current computing capabilities and algorithms for solving the Navier-Stokes equation, the most convenient way to predict the flow-field behavior is the use of Reynolds Averaged Navier-Stokes (RANS) equation. By time averaging the Navier-Stokes equation over a time interval which is much longer than characteristic time-scales of turbulence, unknown terms appear in the time-averaged equations which are Reynolds stresses. The RANS equations include the effect of turbulence through Reynolds stresses. This leads to the closure problem, for which a model is needed to predict the behavior of Reynolds stresses and to close the RANS equation system.

RANS Turbulence models cover a wide range modeling formulation. It in-

volves from algebraic models to more complex algebraic and different Reynolds stress models. Moreover, turbulence models are often calibrated for specific applications. For example, a turbulence model that gives good predictions for attached flows around a single airfoil may produce erroneous results for flow over a multi-element device. Sometimes the errors and discrepancies are not related to turbulence models. Sometimes errors exist in experiments and measurements and one should be ensure about the accuracy of experimental data before compare it with numerical results. In the following four criteria that should be considered before comparing the numerical result with experimental data are presented briefly.

- Errors which are resulted from numerical methods should be less than turbulence model errors. It is easier in this way to judge about the accuracy of turbulence models when they are compared with experimental data [6].
- The accuracy of experimental data should be in an accepted level otherwise errors which are existed in experiments influence our judgement on the accuracy of turbulence models [6].
- Numerical computation should be done with same condition as the experimental data. It means that geometry and flow-field condition of numerical simulation should be the same as the condition in which experiments are conducted [6].
- Prescribing the laminar area should be considered in simulations. Using the assumption of fully turbulent flow is inappropriate in many cases, specially for high lift flows. In this cases the results depend on the location of transition to turbulent and prediction of transition onset may greatly affect the numerical results [6].

2.2 Case setup

2.2.1 General information about the EDGE

EDGE is a parallelized CFD flow solver system for solving 2D/3D viscous/inviscid, compressible flow problems on unstructured grids with arbitrary elements [7]. EDGE is capable of solving the steady state flow as well as performing time-accurate calculations for unsteady flows. This software has also functions for aeroelastic and manoeuvres simulations. Converting the file format, exporting the result for postprocessing are the other facilities

of this software. EDGE solves the Reynolds Averaged NavierStokes compressible equations. Different turbulence models can be used for simulations using eddy viscosity models or using the Explicit Algebraic Reynolds Stress (EARSM) models. More information about the discretization method and convergence acceleration method can be found in reference [7].

Set up the simulation in EDGE software includes four main steps. First, all required information is set in the input file. After that boundary conditions are set based on the physics of the problem. Then *preprocessor* constructs the dual mesh and save all the geometrical data in a file that can be read by flow solver. Finally, flow solver performs the calculations and the obtained results are exported to visualization software to continue on post processing of results.

2.2.2 Mesh information and setup procedure

Figure 2.1 shows the geometry of three-element airfoil which consists of slat, main element and flap.

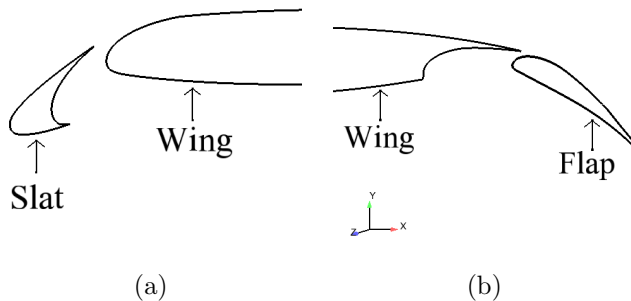


Figure 2.1: Illustration of a three-element airfoil.

In the following a brief description of case setup is presented. The mesh which used in the computation is a hybrid two dimensional mesh consisting of quadrilateral mesh for the boundary layer and a triangle mesh for the domain outside the boundary layer. The total number of the nodes is 204643 and the total number of the element is 323646.

Two different types of boundary conditions can be defined in the Edge solver, weak and strong conditions. In the weak formulation the boundary conditions are imposed through the flux and all unknowns on these boundaries are updated like any interior unknown. In the strong formulation the values of the variables to solve are fixed. these pre-specified boundary values are directly used and not considered as unknowns in the solution [7].

In the present computations, the weak wall boundary condition was used. *Farfield* boundary condition was selected for external boundary condition and weak adiabatic was chosen for the walls. For farfield boundary condition, Characteristic boundary conditions are used. These boundary conditions can be used for both subsonic and supersonic inflow and outflow where the characteristics are either set from free stream quantities for ingoing characteristics or extrapolated from the interior for outgoing characteristics [7]. More details and theory of this type of boundary condition can be found in reference [7].

At an adiabatic wall there is no contribution from the viscous terms to the energy equation since the temperature gradient is zero, $\frac{\partial T}{\partial n} = 0$ and hence the boundary heat flux is set to zero for the total energy equation [7].

In order to solve the flow-field around the multi element airfoil, the Navier-Stokes equations were solved and the air is assumed being calorically gas for low Mach number ($M = 0.15$). Reynolds number $Re = 2.094 \times 10^6$ and the dynamic viscosity was set to 2.92×10^{-5} . Free stream pressure is equal to 100×10^3 . Free stream velocity was calculated based on the free stream temperature and Mach number via the following equation:

$$M_\infty = \frac{q_\infty}{\sqrt{\gamma RT_\infty}} \quad (2.1)$$

where $T = 291.85^\circ K$. From the above equation the free stream velocity $q_\infty = 51.36 m/s$. The velocity decomposed in x and y direction (U_∞ and V_∞ components, and $q_\infty = \sqrt{U_\infty^2 + V_\infty^2}$) are set by considering the angle of attack.

The 2nd order central scheme was chosen for spatial discretization. Since the central scheme cannot recognize the direction of the flow (because of the averaging method), this scheme may become numerically unstable and the oscillation may happen. Therefore, the so-called *artificial dissipation* has to be added for stabilization. In the EDGE this can be done through the terms called VIS2 and VIS4. VIS4 is used for the general numerical dissipation and is set in the present computations to $VIS4 = 0.02 - 0.03$. VIS2 is used for shock discontinuity, of which the function is switched off for low-Mach-number subsonic flows by setting a small value below 0.5. The 2nd-order central scheme, as compared to the upwind differencing methods, introduces less numerical dissipation and is expected to produce better resolution of turbulent variables [8].

2.3 Description of analyzed variables

Mainly two variables are used to analyzed the obtained result from EDGE software, *pressure coefficient* which is shown by C_p and *friction coefficient* which is referred to it as a C_f . In the following, these two variables will be explained. Moreover, *pitching moment coefficient*, C_m , is briefly explained.

2.3.1 Pressure Coefficient

The aerodynamic performance of an airfoil section can be studied through the surface pressure coefficient which is usually expressed as a pressure coefficient C_p [9]. C_p can be explained as a difference between local static pressure and free stream pressure which is normalized by dynamic pressure. The pressure coefficient, C_p , is defined as [10]:

$$C_p = \frac{p - p_\infty}{\frac{1}{2}\rho q_\infty^2} \quad (2.2)$$

For an airfoil, the area between the graph of C_p is the lift coefficient and can be expressed mathematically as the integral of pressure coefficient.

It is possible to present the C_p in term of the velocity for incompressible potential flows [10]. Flow passes over an object with p_∞ and q_∞ . If an arbitrary point in the flow with velocity q and pressure p is selected, using the Bernoulli equation we have:

$$p_\infty + \frac{1}{2}\rho q_\infty^2 = p + \frac{1}{2}\rho q^2 \quad (2.3)$$

The above equation can be written as a follow:

$$p - p_\infty = \frac{1}{2}\rho (q_\infty^2 - q^2) \quad (2.4)$$

By substituting Eq. 2.4 into Eq. 2.2 we will have to following expression:

$$C_p = \frac{p - p_\infty}{\frac{1}{2}\rho q_\infty^2} = \frac{\frac{1}{2}\rho (q_\infty^2 - q^2)}{\frac{1}{2}\rho q_\infty^2}$$
$$C_p = 1 - \left(\frac{q}{q_\infty}\right)^2 \quad (2.5)$$

2.3.2 Friction coefficient and separation phenomena

Flow separation can be traced by the shear stress and adverse pressure gradient.

Shear stress can be expressed as a $\tau = \mu \left(\frac{\partial u}{\partial y} \right)$. Near the wall, shear stress is due to the viscosity and call it as a wall shear stress τ_w . It also known as a surface friction stress or skin friction.[10]. This friction effect can slow down the flow field and, consequently, resulting flow separation.

Another phenomena which leads to separation of the flow is called *adverse pressure gradient*. In this situation pressure is higher downstream of the flow and causes the flow-field to slow down and at the separation point velocity goes to zero and after that flow starts to retard toward the lower pressure region and the flow takes the form of eddies and vortices and create a recirculation region downstream of the surface. Moreover, when the flow starts to slow down the thickness of the boundary layer should be increased in order to satisfy the continuity equation [10].

By knowing the velocity profile of the boundary layer, the surface (or skin) friction can be calculated. The Eq. 2.6 for skin friction stress is based on a non dimension local skin-friction coefficient, the C_f , and has the following form:

$$\tau_w = C_f \frac{1}{2} \rho q_\infty^2 \quad (2.6)$$

where q_∞ is the freestream velocity. Eq. 2.6 can be rewritten based on the C_f . We will have:

$$C_f = \frac{\tau_w}{\frac{1}{2} \rho q_\infty^2} \quad (2.7)$$

The separation phenomena can be analyzed by using the skin friction coefficient. When the flow become detached, the wall shear stress or skin friction stress goes to zero. Hence the C_f will be zero. Some important notes about the C_f can be summarized as the follow:

- C_f is a strong function of Reynolds number, where Re is defined based on the airfoil chord length. The C_f decreases as the Reynolds number increases.
- Magnitude of the C_f depends on the regime of the flow where it is turbulent or laminar. For the same Reynolds number, the C_f has the higher value in turbulent flow in compare with laminar flow.

2.3.3 Pitching moment coefficient

Pitching moment coefficient can be studied in order to have a better understanding of longitudinal static stability. The C_m is defined in Eq. 2.8:

$$C_m = \frac{M}{\frac{1}{2}\rho q_\infty^2 S \bar{c}} \quad (2.8)$$

where M is an aerodynamic moment, S is the plain area and \bar{c} is the wing chord [11]. Pitching moment is, by convention, considered to be positive when it acts to pitch the airfoil in the nose-up direction.

Longitudinal static stability can be expressed as the stability of an aircraft in the longitudinal direction when aircraft is in the established condition. This factor specifies if the aircraft will be able to fly as intended. The low pitching moment coefficient is desirable because it means more stable condition. As this coefficient increases the stability of the aircraft will be reduced.

2.3.4 Prescribed local transition

Local laminar-turbulent transition arises in many aerodynamic application, and its treatment in CFD modeling may greatly affect the simulation accuracy. As it was mentioned before, errors in numerical simulations is not always related to turbulence model itself. the prediction of high-lift flow is sensitive to prescribing the laminar area or considering the effect of transition to turbulence.

Reference [12] categorized the origin of the transition phenomena in to the three types. In aerodynamic application transition happens because of flow instability. Transition happens in turbomachinery because of high level of turbulence in the free stream coming from the upstream blade rows. Finally transition can formed because of the effect of adverse pressure gradient which leads to separation induced transition [12].

Numerical analysis of laminar-turbulence transition can usually be undertaken by means of three major methods, transition prescription, transition prediction and the physical modeling of transitional flow [13]. The approach we follow here is the transition prescription which means the laminar area which has already obtained by theoretical analysis, applied to the RANS flow solver. Therefore, all grid points in the boundary layer upstream of transition line is considered as a laminar flow and downstream of transition line considered as a turbulent flow. Figure 3.30 shows the laminar area around each element of high lift configuration. The laminar region was specified based on the theoretical calculation according to experiment.

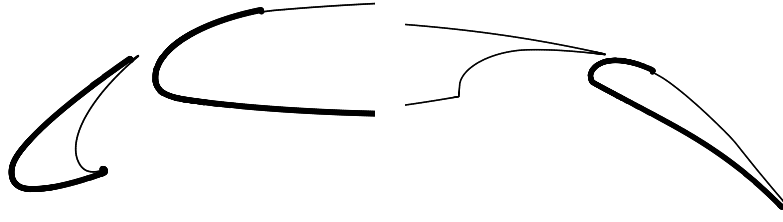


Figure 2.2: Illustration of specified laminar area around the high lift configuration

Depending on the turbulence models used in RANS solver, the laminar area is obtained by manipulating certain turbulence quantities. For algebraic turbulence models, the eddy viscosity μ_t is set to zero in laminar regions, $\mu_{t,lam} = 0$ [14]. For turbulence models with transport equations, the turbulence generation term of the model, S_ϕ , are controlled in such a way that:

$$S_\phi(P)_{lam} = 0$$

where P denotes the current grid point [13].

In EDGE code, the laminar region was obtained by setting the production term in the turbulent kinetic energy equal to zero for two-equation models. For the Spalart-Allmaras (S-A) model, laminar region was obtained by setting the production term in $\tilde{\nu}_t$ equal to zero. Transition was specified via the file that contained the specification of the laminar region, and set in the preprocessor part of the input file.

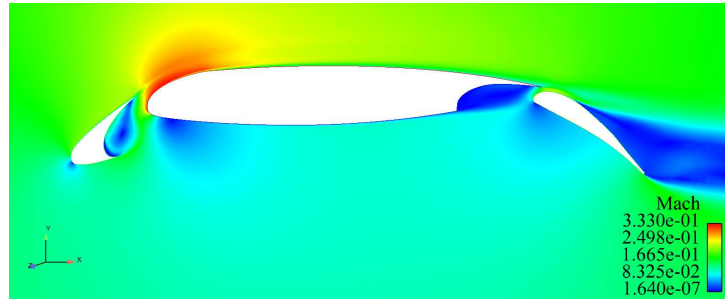
Chapter 3

Numerical Results and discussion

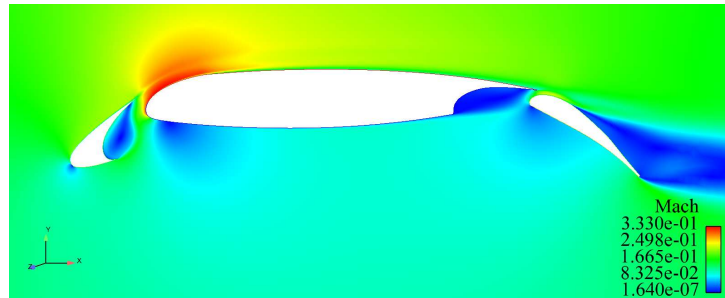
In order to analysis the flow around the high-lift device with different turbulence model, different case have been set up and compared using the EDGE software. The predicted pressure distribution around the multi-element airfoil is first presented and compared with available experimental data. Based on the comparison, several turbulence models are then selected and comparison of the pressure distribution were done for a range of different angles of attack. Another important phenomenon examined in modeling is the flow separation over the flap trailing edge. The friction coefficient was illustrated for different turbulence models and the ability of these models to predict flow separation has been analyzed. Finally we will highlight the velocity field and turbulence viscosity to have a better understanding of turbulence modeling.

3.1 Results at angle of attack, $\alpha = 7.05^\circ$

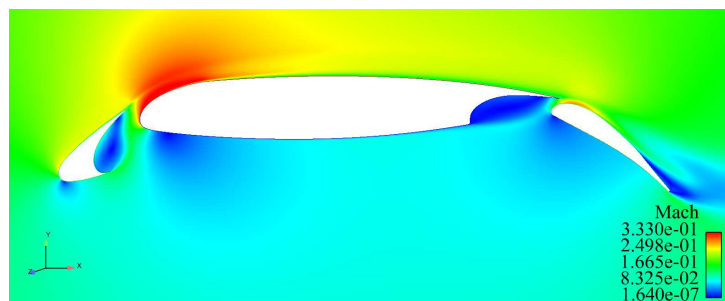
$\alpha = 7.05$ is the angle of attack which is used in the wind tunnel test. Figures 3.1a to 3.1d show the contour plot of Mach number for three turbulence models used for simulation, EARSM + Hellsten $k - \omega$, Menter SST $k - \omega$ and Spalart-Allmaras (S-A) models. It is more convenient to see the behavior of the flow-field around the three element airfoil via the contour plot. The region of high speed flow at the leading edge of the wing can be seen easily. Moreover, the lower part of all elements shows the low speed region also in the separation area near the trailing edge of the flap.



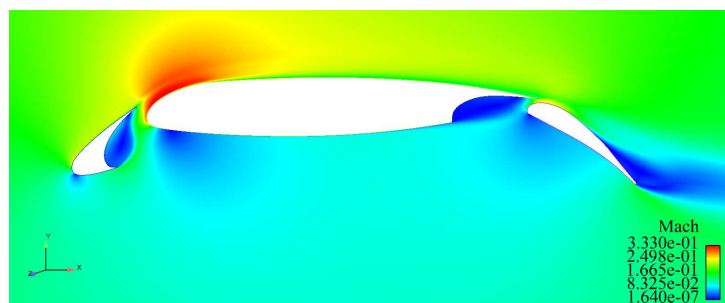
(a) Hellsten $k-\omega$ model



(b) Menter SST model

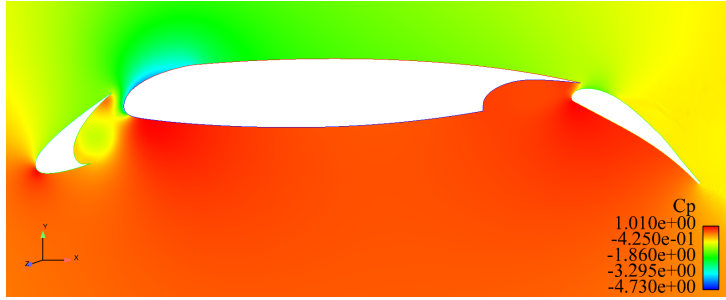


(c) S-A model

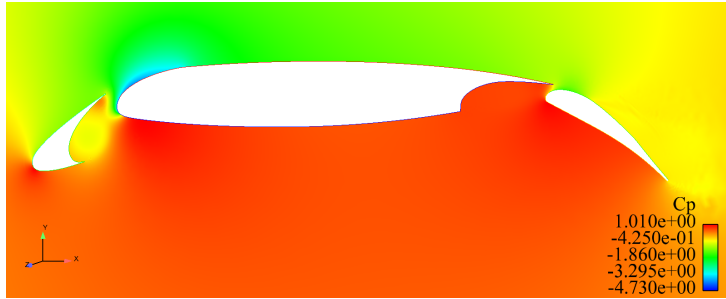


(d) PDH model

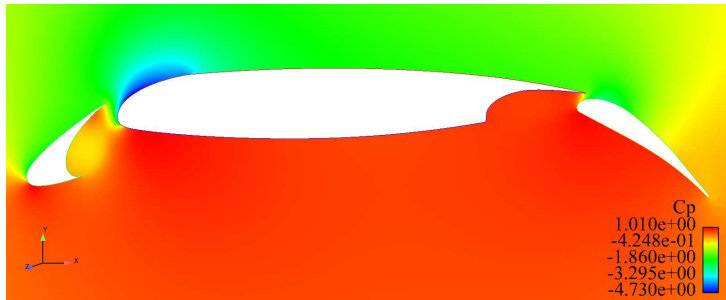
Figure 3.1: Contours of Mach number for four turbulence models



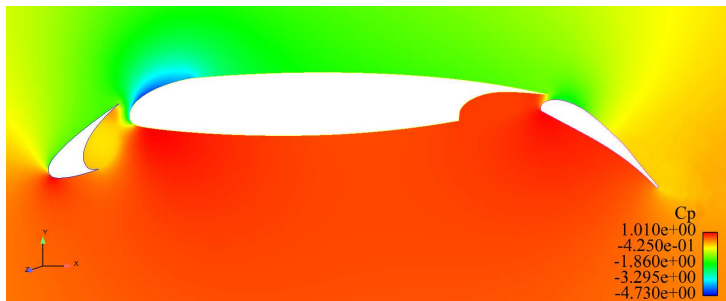
(a) Hellsten $k-\omega$ model



(b) Menter SST model



(c) S-A model



(d) PDH model

Figure 3.2: Contours of pressure coefficient C_p for four turbulence models

The pressure distribution is depicted in Figures 3.2a to 3.2d. The low

pressure area at the leading edge of the wing and generally over the upper surface of the wing is obvious. These contour plots are useful to understand the physics of the problem and general behavior of the flow. The more exact analysis is done by focusing on the aerodynamic coefficients like C_p and C_f and the flow-field is analyzed through these variables.

Figure 3.3 shows the surface pressure coefficient distribution around the multi-element airfoil. The angle of attack for this case is equal to 7.05° and results obtained with the S-A model, the EARSM + Hellsten $k - \omega$ and the Menter SST turbulence models with fully turbulent assumption are shown and compared with the experimental data. Surface pressure coefficient distribution is displayed for the three elements in the same Figure and the x direction is normalized by the retracted chord length.

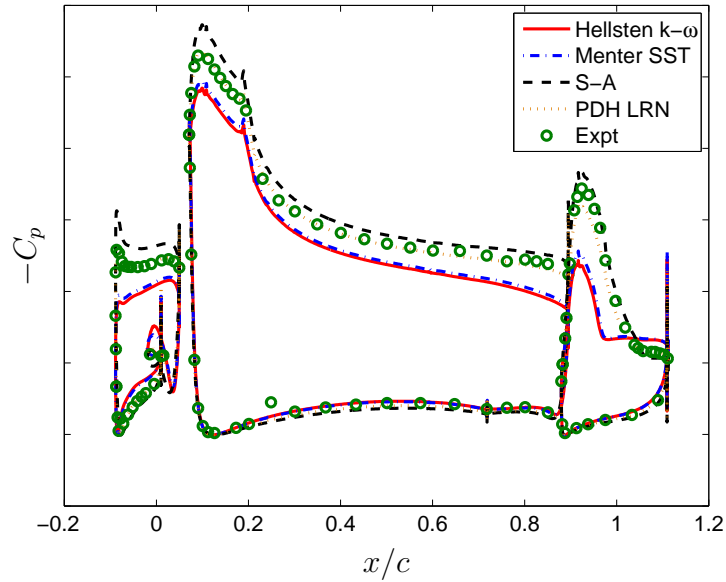


Figure 3.3: Comparison of pressure coefficient for different turbulence models, $\alpha = 7.05^\circ$

The C_p is plotted with negative values, so the upper surface of the airfoil corresponds to the upper part of the curve. It can be understood from Figure 3.3 that C_p starts from one at the stagnation point and after that it increases on both upper and lower parts of the airfoil (pressure decreases). The peak on the pressure distribution graph corresponds to the maximum value of the velocity. The region after the peak is called pressure recovery region. In this region pressure starts to increase from its minimum value; this region also corresponds to the adverse pressure gradient region. The adverse pressure

gradient may lead to boundary layer separation [9] as we will discuss in detail later. The pressure distribution around the trailing edge is related to the shape and thickness of the airfoil trailing edge.

In general, computed pressure on the upper surface of the slat in Figure 3.3 for S-A model is lower than the experimental values but the tendency of pressure profile for S-A model is more accurate in comparison with other models. The EARSM + Hellsten $k - \omega$ and The Menter SST models predict higher suction pressure in comparison with experimental data. Note that the S-A model solution shows a higher suction peak in $-C_p$ than the other two models which are based on the $k - \omega$ formulation. This difference is largely responsible for the differences in predictions of drag and lift. The obtained result from PDH LRN model shows a good agreement with experimental data on both upper and lower part of the slat. The slat produces a thrust force since it is deflected downward and the suction surface faces forward. However, higher computed suction level on the flap pull in the opposite direction, partially canceling the slat contribution.

Table 3.1: Comparison of drag coefficient for different turbulence models at $\alpha = 7.05^\circ$

Coefficient	element	Models			
		S-A	Menter SST	Hellsten k- ω	PDH
C_d	slat upper part	-0.192	-0.108	-0.10	-0.15
	slat lower part	0.0055	0.035	0.038	0.020
	Total	-0.18	-0.072	-0.062	-0.136

Table 3.1 shows the comparison of drag force of the slat for the S-A model, the Hellsten $k - \omega$ model and the Menter SST model.

On the lower side of the slat, the S-A model predicts lower pressure than the experimental data. The Hellsten $k - \omega$ model and Menter SST model predict higher pressure in comparison with experimental data. Moreover, the location of the stagnation point is not the same for all of the turbulence models. Stagnation point of the S-A model is located rearward in comparison with the other two models as can be seen from Figure 3.4.

The main-element (wing) pressure distribution has a large suction peak near the leading edge followed by a pressure recovery region and then leveling off into a flap suction side. Note that the pressure does not recover back to

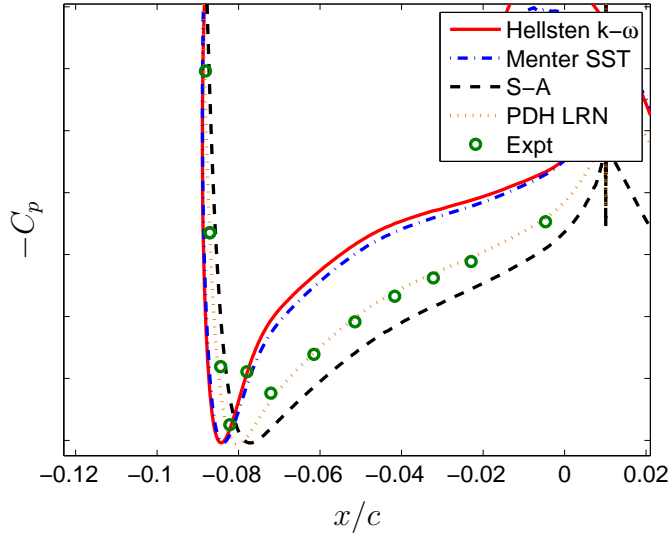


Figure 3.4: Stagnation point on the slat for different turbulence models, $\alpha = 7.05^\circ$

the freestream level since the trailing edge is adjacent to the flap suction peak. The same trend as for the slat is observed here. The S-A model predicts lower pressure on the upper surface of main element, whereas the other $k - \omega$ models predict higher suction pressure on the upper surface in comparison with the experimental data. This difference is more obvious near the leading edge of the main element. The acceleration of the flow predicted by S-A model is stronger than the Hellsten $k - \omega$ and the Menter SST models. The PDH LRN model has predicted a flow field that is more consistent with experimental observation, as compared with the other models considered.

This over-prediction of the suction peak correlates with values predicted for the lift coefficient. The S-A model which produces the highest suction peak, yields the highest value for the C_l . The Hellsten $k - \omega$ model which predicts the lowest suction peak, yields the lowest value for the C_l . Table 3.2 shows the obtained values for lift force and lift coefficient for different turbulence models.

Finally, on the flap region pressure distribution shows the peak on the leading edge and as it was mentioned previously, a high suction level of pressure on the flap will cancel the thrust effect of the slat and pull in the opposite direction. Predicted suction peak on the flap is higher for S-A model and other models predicted higher surface pressure distribution in compare with experimental data. Another interesting phenomenon which can be explained through the pressure distribution is the flow separation.

Table 3.2: Comparison of lift coefficient for different turbulence models and $\alpha = 7.05^\circ$

Variable	Element	Models			
		S-A	Menter SST	Hellsten $k-\omega$	PDH
C_l	Slat	0.31	0.19	0.18	0.26
	Wing	2.44	2.00	1.95	2.27
	Flap	0.40	0.28	0.26	0.34
	Total	3.16	2.47	2.40	2.87

The pressure distribution on the flap, as shown in Figure 3.3 reveals that onset of flow separation takes place at different location upon the turbulence model used. When the line of the pressure distribution become constant it means that the flow is separated from the surface. This phenomena will be discussed in detail in the following.

It is important to understand the contribution of the viscosity and pressure in lift and drag coefficient. Table 3.3 shows contribution of these variables in lift and drag coefficient. A comparison is made for lift and drag coefficients predicted by three different turbulence models. The angle of attack $\alpha = 7.05^\circ$ and free stream Mach number $M = 0.15$.

Figure 3.5 shows the distribution of skin friction coefficient around the multi-element airfoil. An observation of the skin friction in the upper part is more interesting, since the boundary layer separation occurs on the upper surface and the simulation of boundary layer is often more sensitive to turbulence modeling.

It can be seen clearly from Figure 3.5 that the C_f predicted by S-A model is higher than by the other two models. It means that S-A model predicts higher wall shear stress than the other two $k - \omega$ models. At high Reynolds number, say 10^6 , skin friction drag is relatively small, for example in order of 10^{-2} here.

The C_f distribution in Figure 3.5 display an expected trend starting from high value at the leading edge due to the high velocity flow and thin boundary layer. After this region and moving further down, the values of C_f is decreasing due to the increase in boundary layer thickness and reducing the flow velocity. It is expected that the C_f drops near the trailing edge of the

Table 3.3: Contribution of pressure and viscosity in the lift and drag coefficient for different turbulence models, $\alpha = 7.05^\circ$

Coefficient	Component	Models		
		S-A	Menter SST	Hellsten k- ω
C_l	viscous part	0.00142	0.00155	0.00169
	pressure part	3.16	2.47	2.40
	Total	3.16	2.47	2.40
C_d	viscous part	0.143	0.0114	0.0116
	pressure part	0.0439	0.0641	0.0646
	Total	0.0583	0.0756	0.0762

main element but because the suction peak of the flap is located near the trailing edge of the main element, it keeps the trailing edge velocity large and have produced a flat C_f distribution.

The last part of the C_f distribution located approximately between $x/c = 0.88$ to $x/c = 1.1$ is the distribution of skin friction coefficient around the flap. As it was mentioned before, when distribution of pressure coefficient around a body becomes constant, the flow is separated. This phenomenon can be understood better by looking at skin friction coefficient. When the flow-field becomes detached, the wall shear stress goes to zero. Separation point is the location where $C_f = 0$ and negative value of C_f indicates the subsequent separation bubble. Again, we take a closer look at the pressure distribution on the flap which is shown in Figure 3.6. Figure 3.6 shows that the two turbulence models based on the $k - \omega$ approach predict an early separation on the flap approximately at $x/c = 0.97$ and there is a poor agreement between numerical result and experimental data. However, the result of S-A model is more consistent with experimental data and it predicts the separation at $x/c = 1.07$.

By means of Equation 3.1 and Figure 3.5 the separation length is estimated:

$$L_s = \frac{X_{tf} - X_{sf}}{X_{tf} - X_{lf}} \quad (3.1)$$

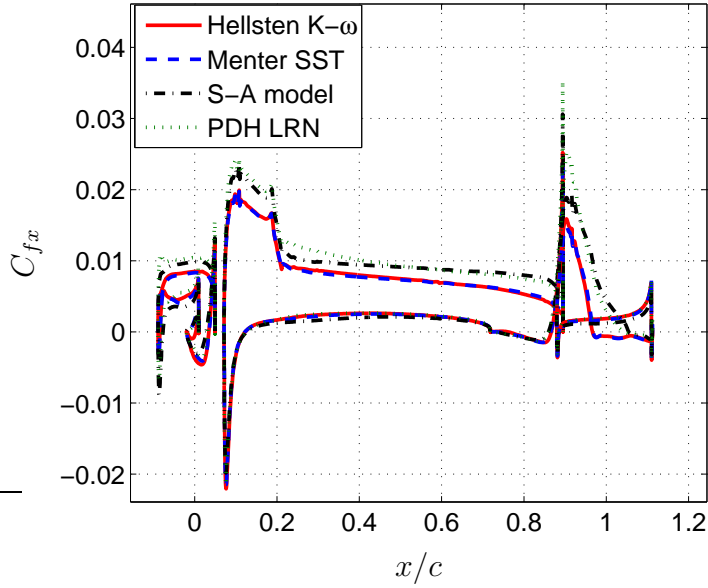


Figure 3.5: Comparison of skin friction coefficient in streamwise direction for different turbulence models. $\alpha = 7.05^\circ$

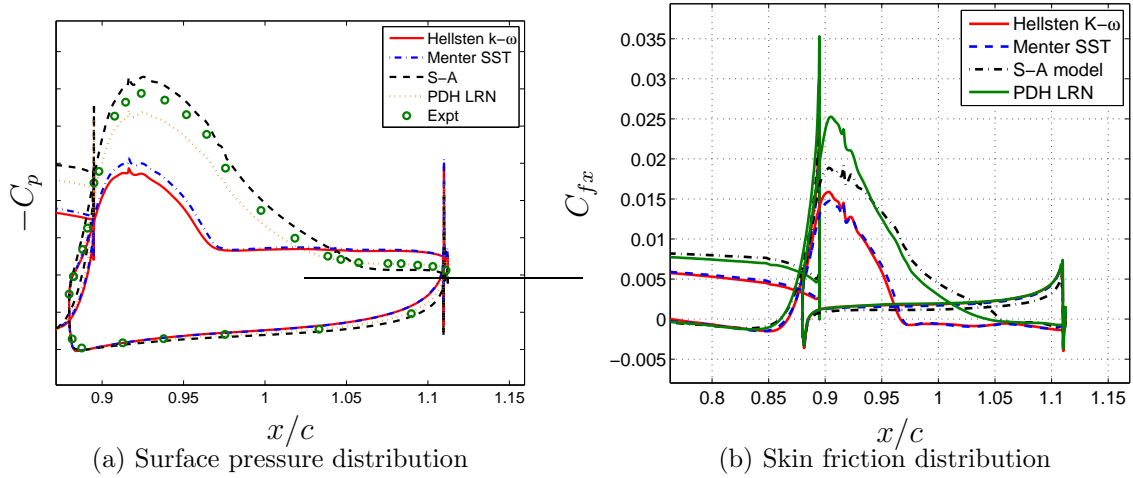


Figure 3.6: C_p and C_f over the flap, $\alpha=7.05^\circ$

X_{tf} : x-coordinate at the flap trailing edge.

X_{lf} : x-coordinate at the flap leading edge.

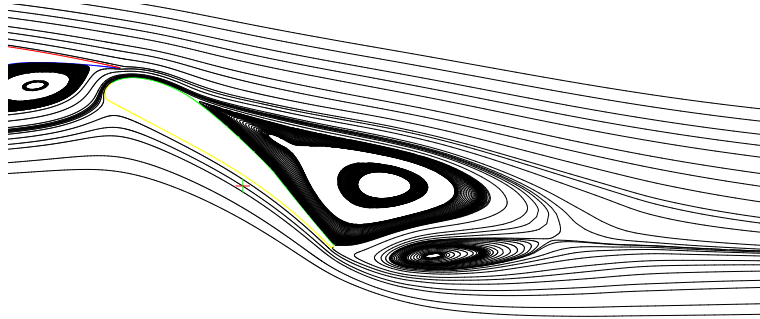
X_{sf} : x-coordinate at the flap separation point.

Table 3.4: Flow separation on the flap based on the flap chord

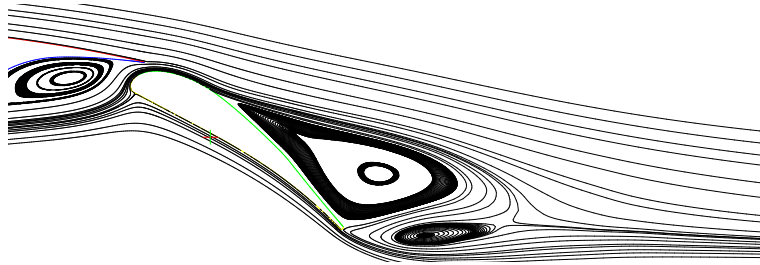
Experiment	Models			
	S-A	PDH LRN	Menter SST	Hellsten $k-\omega$
–	25%	29%	64%	65%

The results are summarized in table 3.4. These values indicate the separation length from the trailing edge of the flap. As can be seen from table 3.4, S-A model predicted the smallest reverse flow area in compare with the other models. This fact can be seen better from the velocity streamlines over the flap which are displayed in Figure 3.7 for different turbulence models.

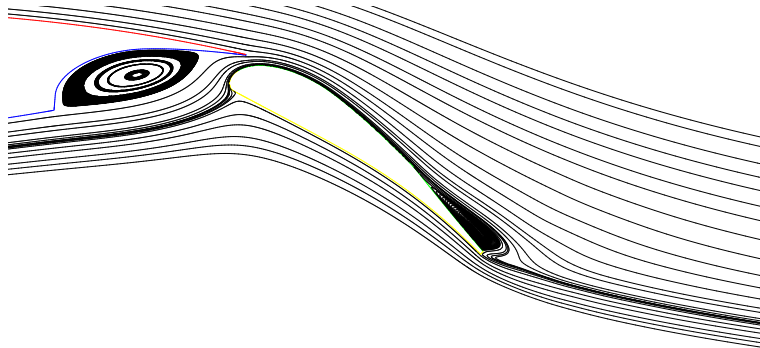
Figure 3.7 shows the separation bubbles on the flap for different the turbulence models. It is obvious from Figure 3.7 that the recirculation zone predicted by S-A model is the smallest one between these models. Hence, the surface pressure on the suction side computed by the S-A model is the highest among these models. The Hellsten $k - \omega$ model predicts the largest recirculating area and separation starts from 35% of the flap chord length from the leading edge which is not in agreement with experiment. Therefore, pressure distribution obtained from this model has the lowest value between these models. However, because of the lack of experimental data for the skin friction coefficient, C_f , it is difficult to judge about the superior turbulence model in predicting the adverse pressure gradient. However, by looking at the pressure distribution around the flap, Figure 3.6, it can be seen that the S-A model result is more consistent to experimental data near the trailing edge of the flap where the flow becomes separated. Therefore, it seems that the S-A model predicts the separation better than the other two turbulence models which are based on the $k - \omega$ formulation.



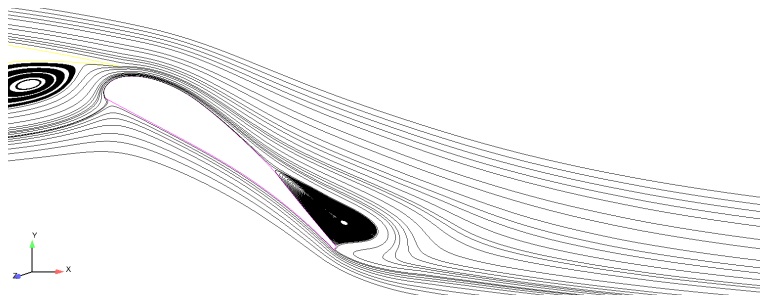
(a) Hellsten $k-\omega$ model



(b) Menter SST model



(c) S-A model



(d) PDH LRN model

Figure 3.7: Illustration of streamlines obtained from different turbulence models over the flap

3.2 Effect of changing the angle of attack

Another comparison was made for different angles of attack using the same turbulence models. For this case three different angles of attack are chosen: 6.75° , 7.05° and 7.5° . The other variables like Mach number and Reynolds number did not change.

Based on the test case description of the present high-lift device prepared by DLR, it was mentioned that for incidence angles α smaller or equal to 9° the flow remains attached on the wind tunnel side walls until the position on the flap where separation occurs. Therefore, the correction of the angle of attack to take into account the effects of the wind tunnel side walls for numerical simulation in 2D are less than 1° . In order to find the correct angle of attack a series of RANS simulation were performed. Experimental data is obtained for the angle of attack equal to 7.05° hence, the correction for angle of attack was done based on the mentioned criteria and angles of attack at 6.75° , 7.05° and 7.5° were selected and the comparison of pressure coefficient for different angles of attack with experimental data are shown in figures 3.8, 3.10 and 3.11.

However, recently it was proposed by DLR that the angle of attack at 6° is the corrected angle by considering the effect of the wind tunnel side wall. Hence, the simulations were repeated for new angle of attack and the results are shown in Figures 3.12 and 3.13.

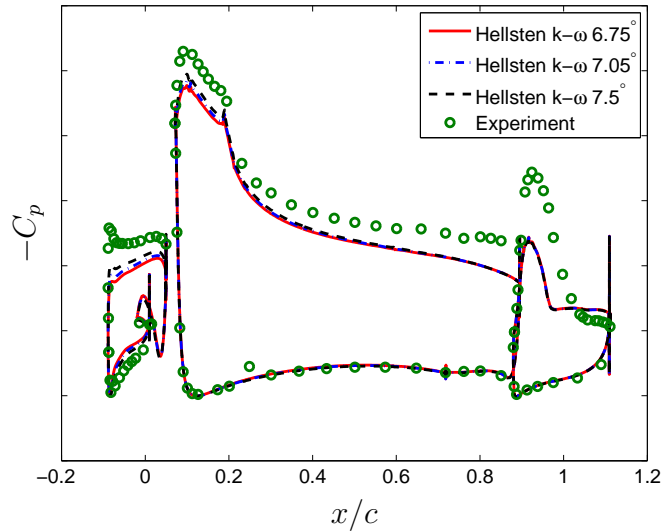


Figure 3.8: Comparison of surface pressure distribution

From Figure 3.8 it can be understood that when the angle of attack is

increased, the suction peaks will increase. It means that the area under the graph of C_p is increasing and this will lead to higher lift force. Moreover, pressure coefficient varies more on the top of the airfoil than on the lower part and the most noticeable part is the leading edge of the slat and the main wing. In these parts the flow accelerated because of the favorable pressure gradient, the pressure decreases and the flow-field velocity increases.

As the α , angle of attack of the three-element airfoil is increased, the point of minimum pressure (suction peak) moves toward the leading edge. The pressure increases along the streamwise direction. The resulting adverse pressure gradient may induce boundary layer separation. The flow separation significantly modifies the pressure distribution along the surface and, consequently, the lift and drag characteristics.

Suction pressure level of the flap upper surface in Figure 3.8 did not change significantly from the $\alpha = 6.75^\circ$ to $\alpha = 7.5^\circ$. Since flap is located in the downwash from the main element, its local angle of attack stays nearly constant throughout the range of angles of attack considered in this report.

The stagnation location greatly affects the suction peak. This can be seen in the slat pressure distribution where the solutions with the higher suction peaks have a more rearward stagnation point. Small errors in the stagnation point prediction can lead to large suction differences. A high resolution mesh around the stagnation point can prevent the mentioned problem.

Stagnation point is changed by changing the angle of attack. At large angles of attack the stagnation point moves further downstream to the lower side of the airfoil and increases the pressure on the lower surface [11]. This fact can be well understood by looking at figures 3.9a and 3.9b which shows the stagnation point on the slat for angle of attack at 6° and 7.5° respectively.

Figures 3.10 and 3.11 show the surface pressure distribution for the Menter SST and S-A models.

The behavior of the Menter SST and the Hellsten $k - \omega$ models are different in comparison with the S-A model. The first two mentioned model under predicted the suction peak and hence, in order to find the corrected angle of attack based on the wind tunnel side wall effect, angle of attack should be increased which increases the adverse pressure gradient effect and therefore, these models are not suitable for conducting further simulations. However, S-A model over predicted the suction peak and by reducing the angle of attack it will be possible to find the corrected angle of attack based on the wind tunnel side wall effect. Figure 3.12 shows the surface pressure distribution for angle of attack of 6° . The obtained numerical results are in good agreement with experimental data.

The same procedure has been taken for the PDH LRN model and the results are displayed in Figure 3.13. The obtained result for this models

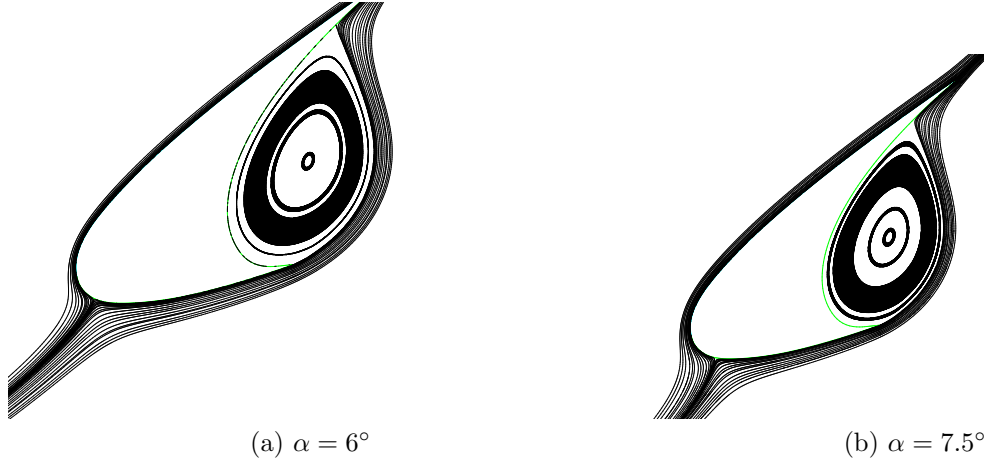


Figure 3.9: Stagnation point on the slat for $\alpha = 6^\circ$ and $\alpha = 7.5^\circ$ for S-A model

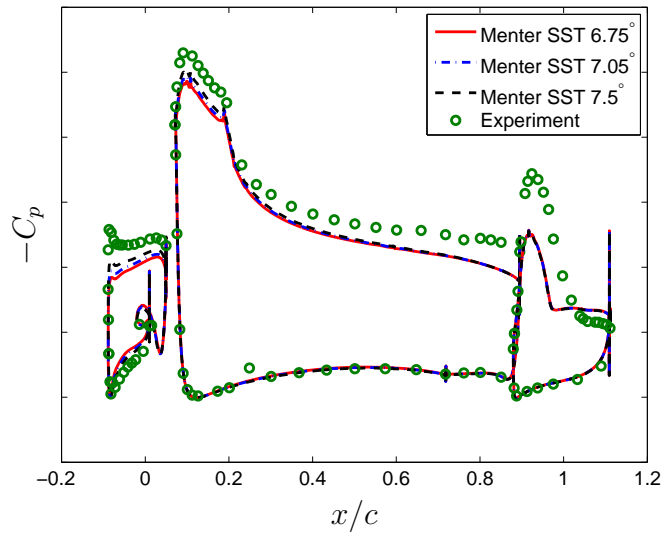


Figure 3.10: Comparison of surface pressure distribution

shows that surface pressure distribution under predicted when angle of attack equal to 6° is chosen. Prescribing the laminar area in this case might improve the consistency with experimental data.

Changing the angle of attack also has an effect on the lift and drag coefficient. Table 3.5 shows values of C_l , C_d and C_m for the three turbulence models and different angle of attack which were examined for this case.

Figure 3.14 shows the distribution of skin friction coefficient which is obtained from the Hellsten $k - \omega$ model for three different angles of attack.

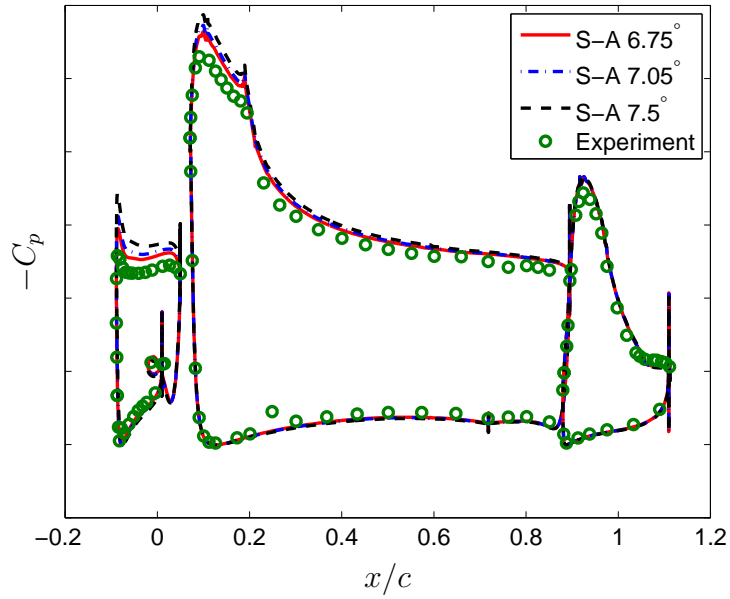


Figure 3.11: Comparison of surface pressure distribution

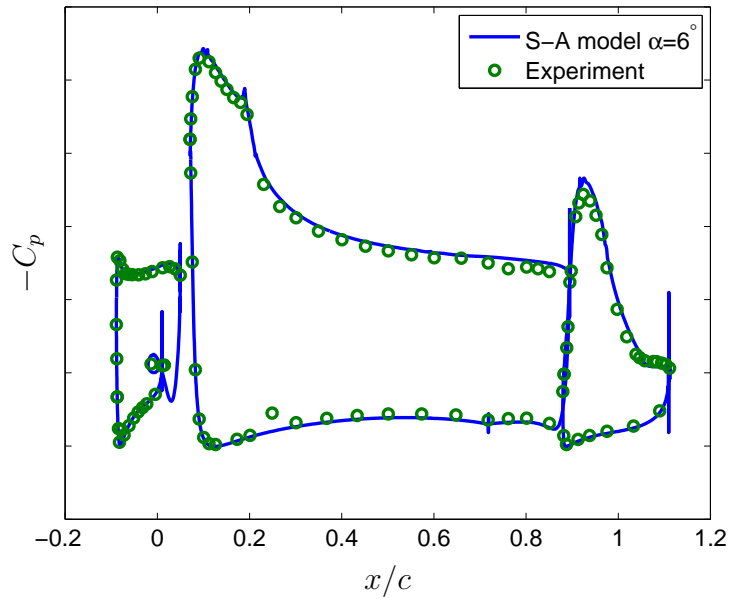


Figure 3.12: Surface pressure distribution for S-A model $\alpha = 6^\circ$

C_f rapidly increases from a negative value at the stagnation point to a peak shortly down stream of the leading edge. This rapid increase is due to the

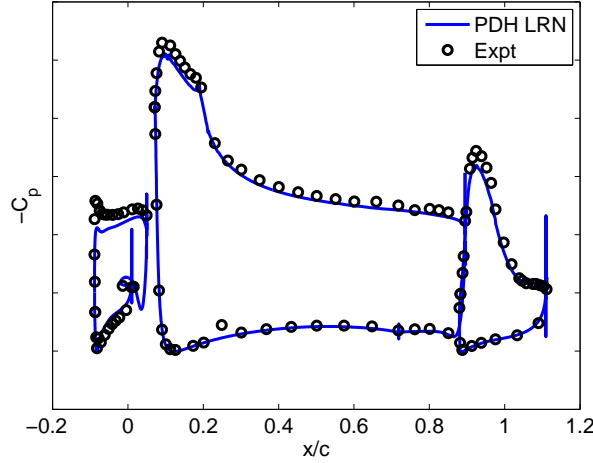


Figure 3.13: Surface pressure distribution for PDH LRN model $\alpha = 6^\circ$

Table 3.5: Comparison of lift and drag coefficient for different angles of attack

Coefficient	α	Models		
		S-A	Menter SST	Hellsten $k - \omega$
C_l	$6.75^\circ\alpha$	3.12	2.43	2.37
	$7.05^\circ\alpha$	3.16	2.47	2.40
	$7.5^\circ\alpha$	3.23	2.52	2.45
C_d	$6.75^\circ\alpha$	0.058	0.075	0.076
	$7.05^\circ\alpha$	0.058	0.075	0.076
	$7.5^\circ\alpha$	0.059	0.076	0.077

rapidly increasing velocity as the flow over the boundary layer expands around the leading edge. After the peak, C_f starts to decrease uniformly. It was the general behavior of the C_f graph.

Value of C_f at the angle of attack equal to 7.5° is higher than the other angles of attack at the leading edge, but the tendency is vice versa at the trailing edge. The value of C_f at the angle of attack 7.5° is smaller than the other two angles of attack. Figure 3.15a and Figure 3.15b show a zoom of C_f

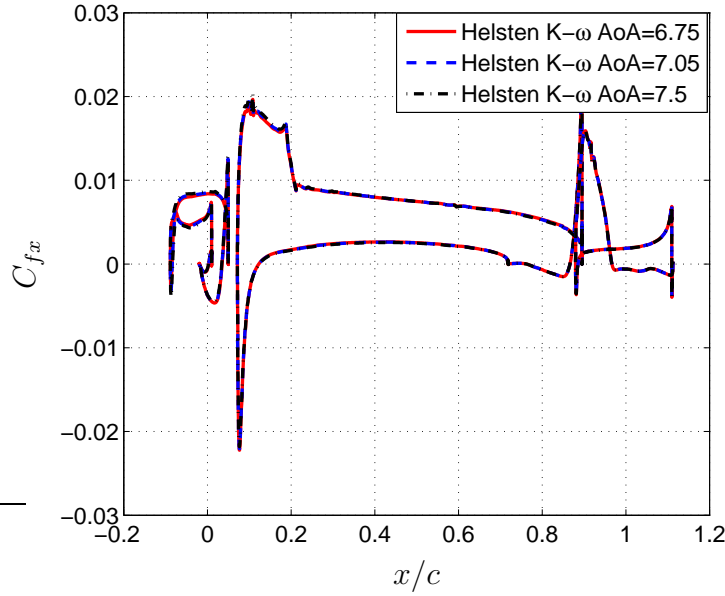


Figure 3.14: Comparison of friction coefficient in streamwise direction.

at the leading edge and the trailing edge. However, when the angle of attack is changed, the differences between the obtained results for C_f at different angles of attack is not as sensible as the C_p . Figures 3.16a and 3.16b show the distribution of skin friction coefficient for S-A model and Menter SST model. As it can be seen from these figures, changing the angle of attack does not have a considerable effect on C_f .

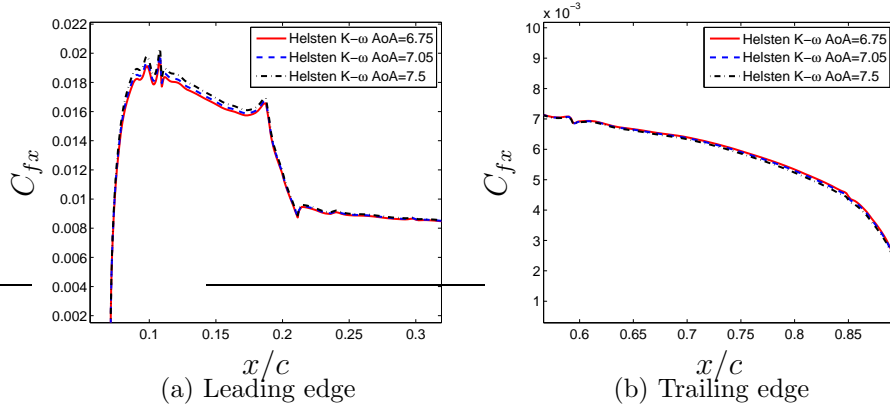


Figure 3.15: Friction coefficient in streamwise direction for Hellsten $k-\omega$ model

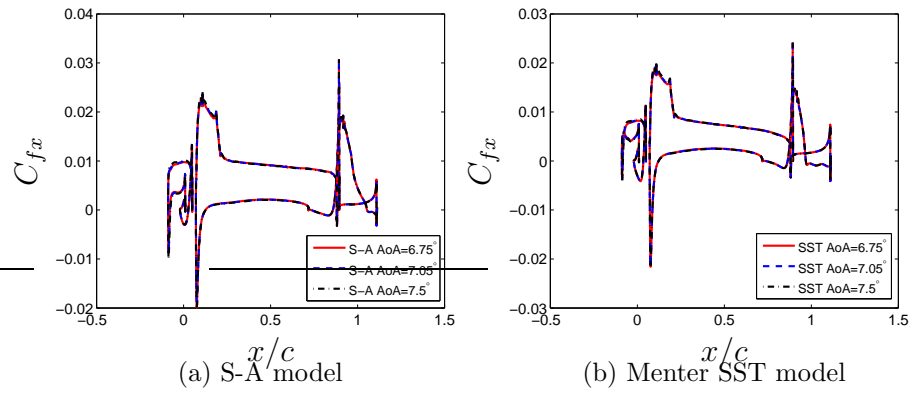


Figure 3.16: Friction coefficient in streamwise direction for S-A model and Menter SST model

3.3 Computation with Local prescribed transition

The computation in the present report have been carried out for Reynolds number $Re = 2.094 \times 10^6$ and $\alpha = 7.05^\circ$. Here the obtained results with local prescribed transition for different turbulence models are compared with fully turbulent assumption results and difference will be explained.

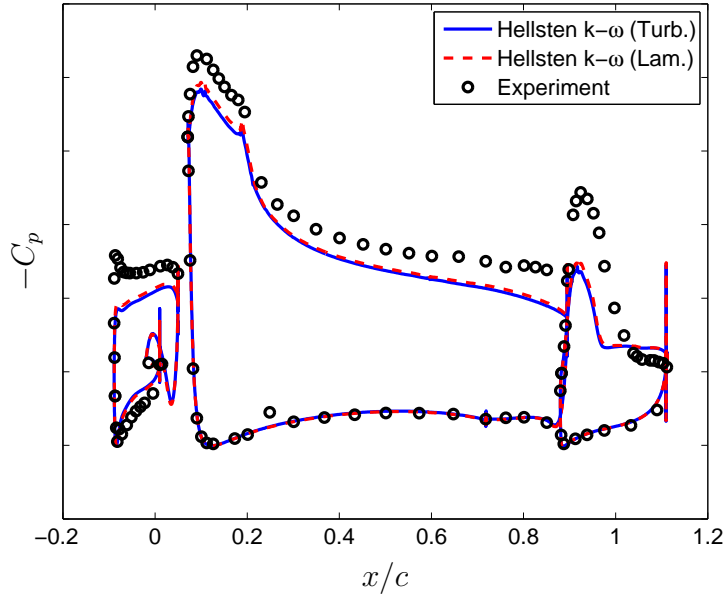


Figure 3.17: Comparison of surface pressure distribution

Figures 3.17 and 3.18 show the pressure distribution around the multi-element airfoil for the Hellsten $k - \omega$ model and the S-A model. Angle of attack for this case $\alpha = 7.05^\circ$ and the other variables are the same as the previous simulations. As we expected, the suction peak which is obtained by laminar prescribed transition is higher than fully turbulent assumption because of the existence of a laminar region. The agreement between the experimental data and numerical simulation is improved when the assumption of laminar-turbulent transition is incorporated into the simulation. In Figure 3.17 the suction peaks on the main element and the flap are increased, but still under predicted by Hellsten $k - \omega$ model. However, there is no big difference in the obtained result from the Hellsten $k - \omega$ with fully turbulent assumption and with the local prescribed transition and they match in a large part of the main airfoil and the flap. There is a small difference

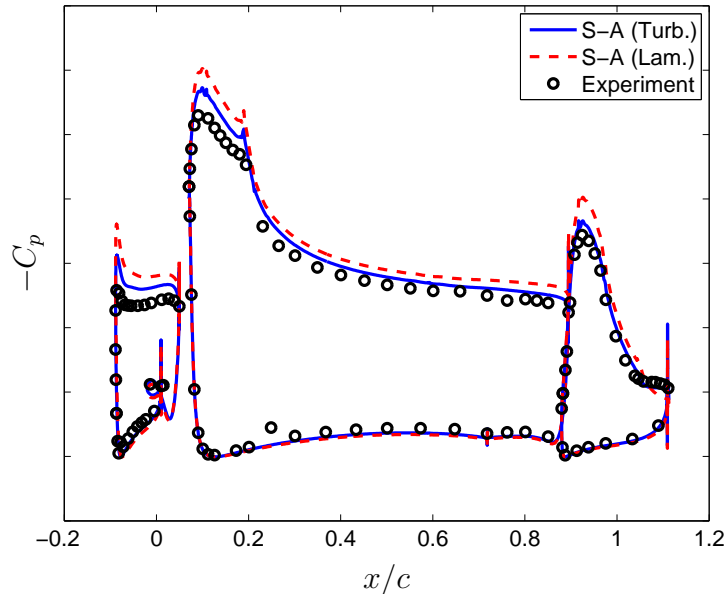


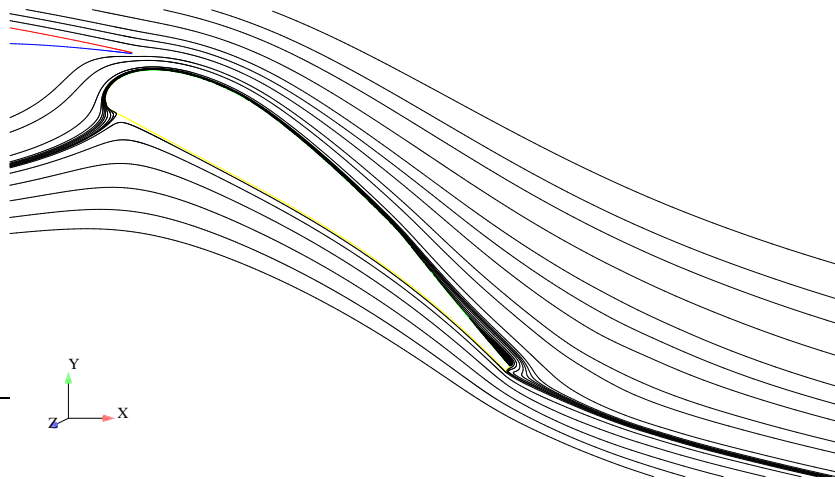
Figure 3.18: Comparison of surface pressure distribution

in predicted separation point when laminar area is prescribed in comparison with fully turbulent assumption. The computation with prescribed local transition shows an early separation in comparison with the full-turbulence simulation.

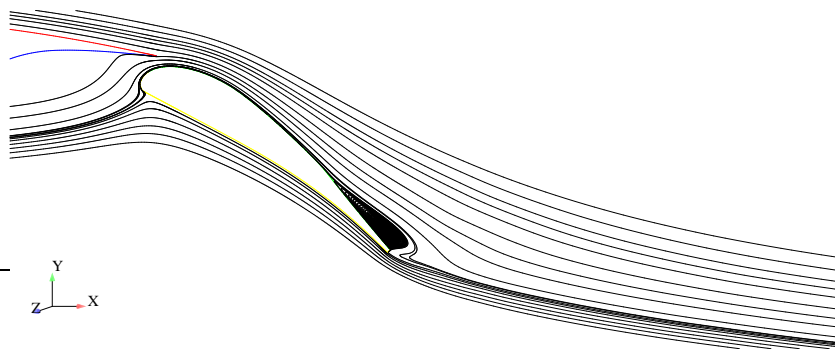
Figure 3.18 shows the pressure coefficient for the S-A model. Larger values for the pressure coefficient are obtained by assumption of local prescribed transition, but the differences between the experimental data and transition calculation is more considerable than the Hellsten $k - \omega$ model. The suction peaks on all elements is over estimated and the results quantitatively does not agree well with the experiment on the slat and the main airfoil, and even exhibits higher deviations than the C_p distribution with a fully turbulent computation, especially on the upper side. The reason can be explained by considering the selected angle of attack. The angle of attack 7.05° was measured in wind-tunnel test, which needs to be corrected in computations with free flight conditions as in the present work. The discrepancies may be reduced if a corrected and smaller angle of attack is used.

The predicted flow separation over the flap trailing edge is changed for the S-A model when the assumption of local prescribed transition is used. When laminar-turbulent transition is prescribed, the separation point is delayed and becomes closer to the trailing edge. Moreover, the separation length is smaller than the case of fully turbulent assumption. Figure 3.19 shows

the separation on the flap for transition computation and fully turbulent computation.



(a) Transition computation



(b) Fully turbulent computation

Figure 3.19: Comparison of recirculation area over the flap for the S-A model

Another turbulence model which is used to investigate the effect of laminar-turbulent transition is the Menter SST model. Figure 3.20 shows the distribution of pressure around the multi-element airfoil for angle of attack $\alpha = 7.05^\circ$ and obtained results for fully turbulence and transition computations are compared with experimental data.

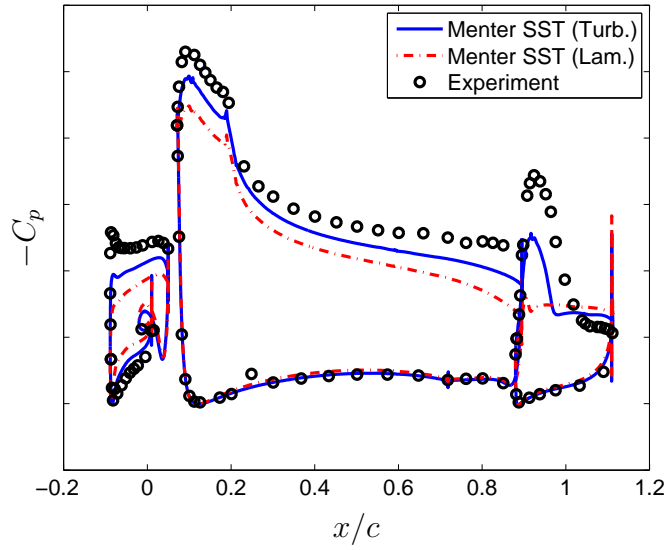


Figure 3.20: Comparison of surface pressure distribution

As it can be seen from Figure 3.20, the C_p distribution does not agree well with experimental data over all elements and deviation from experimental data is increased considerably. The error in the result with prescribed local transition is larger than the fully turbulent computation. This is related to the prediction of flow separation on the flap. The flow-field is totally separated over the flap when the assumption of transition is used. This large separation affects the whole flow-field upstream and leads to a higher pressure distribution around all elements of the high lift configuration. Figure 3.21 shows the velocity streamlines around the flap and separation points and separation lengths are compared for these two assumption.

Another turbulence model used to study the effect of prescribed transition is the PDH LRN $k - \omega$ model which is a low Reynolds number model. Figure 3.22 shows the distribution of pressure around the three-element airfoil which is obtained by PDH low Reynolds number model. The obtained result with PDH model is much better than the Hellsten $k - \omega$ and Menter SST models and there is a good agreement between experimental data and numerical results. Better result are obtained for the suction peak pressure on the flap by assuming the local prescribed transition and the numerical results are more consistent with experimental data on the upper part of the flap. However, suction peak is over predicted on the wing and the flap when the assumption of local prescribed transition is used. In this case the obtained result by the assumption of fully turbulent is more consistent to experimental data than

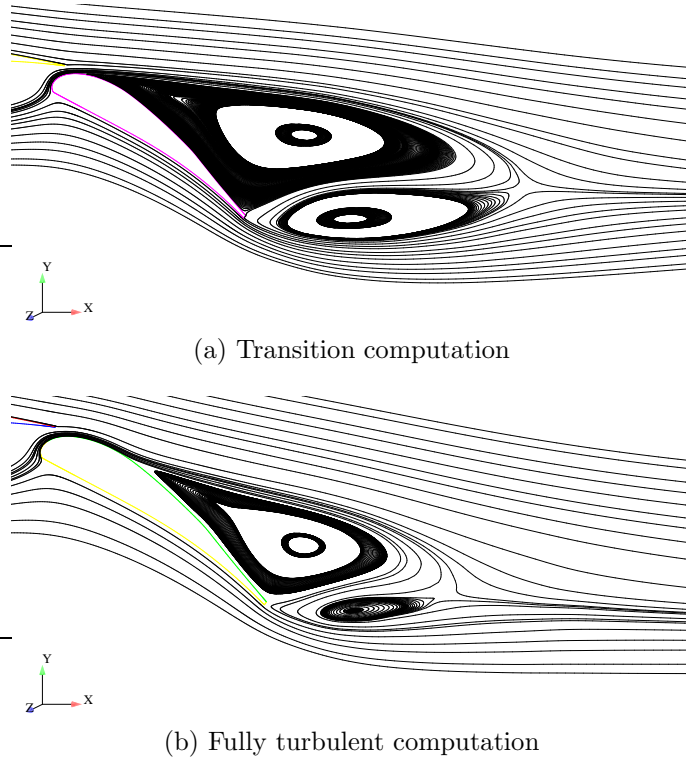


Figure 3.21: Comparison of recirculation area over the flap for the Menter SST model

the result of the local prescribed transition.

Table 3.6 compares the coefficients of lift and drag obtained by fully turbulent computation and transition calculation. The general trend is that the lift coefficient increases and the drag coefficient decreases when laminar area was specified, which is the expected result. However, the Menter SST model has produced results in fairly large discrepancies, for which the lift coefficient decreases and the drag coefficient increases when laminar area was specified. The main reason is related to the prediction of flow separation over the flap, as discussed above.

So far, we analyzed the effect of laminar-turbulent transition via the pressure coefficient, C_p , but the friction coefficient, C_f , also reveals interesting features of the flow. Figure 3.23 shows a comparison of the skin friction coefficient with fully turbulent computation and computation with transition for the Hellsten $k - \omega$ turbulence model. For this case, Mach number $M = 0.15$, the Reynolds number $Re = 2.094 \times 10^6$ and angle of attack $\alpha = 7.05^\circ$.

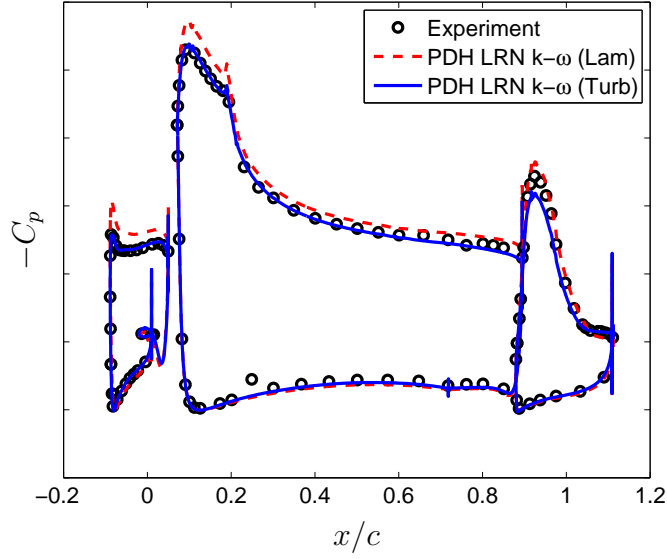


Figure 3.22: Comparison of surface pressure distribution

Table 3.6: Comparison of the lift and drag coefficient for fully turbulent assumption and specified local transition

Coefficient	Model	Assumptions		
		Fully turbulent	Prescribed trans.	Difference
C_l	S-A	3.16	3.38	7%
	Hellsten k- ω	2.40	2.46	2.5%
	Menter SST	2.47	2.08	-15%
	PDH lrn	2.89	3.14	8.6%
C_d	S-A	0.058	0.047	18.8%
	Hellsten k- ω	0.076	0.069	8.5%
	Menter SST	0.075	0.098	-30%
	PDH lrn	0.069	0.054	20%

The reduction of skin friction coefficient over the slat is more considerable than the other parts because the laminar area was prescribed over both the

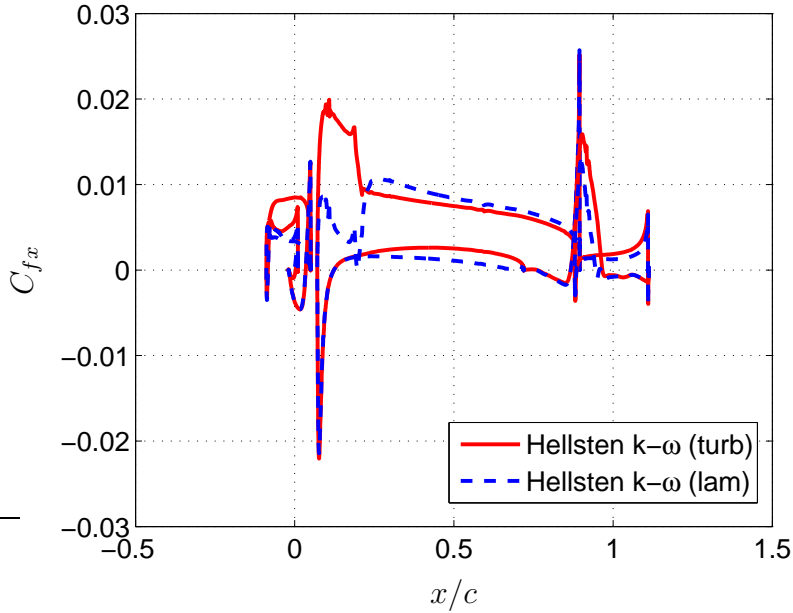


Figure 3.23: Comparison of skin friction coefficient in streamwise direction.

upper and lower parts. The behavior of the C_f is more interesting over the wing. At the leading edge of the wing, skin friction coefficient reduces and the flow accelerates more than in the case where assumption of fully turbulent flow was used. It means that the peak suction pressure will increase to a higher value. This fact has already been shown in Figure 3.17. After the region where the C_f is reduced there is a sudden increase in the C_f at $x/c = 0.19$ approximately. This sudden change or sudden increase, shows the transition onset to turbulent boundary layer, the turbulent kinetic energy is increasing and the skin friction drag starts to increase because the regime of flow is changed from laminar to turbulent. After the transition point, turbulent boundary layer develops downstream.

Figure 3.23 shows also that, by prescribing the laminar region, the development of the boundary layer over the wing is affected. The difference in the wall shear stresses obtained, respectively, in the calculations with local transition and with full-turbulence assumption suggests that the gradient of velocity $\frac{\partial u}{\partial y}$ at the wall has a different slopes. This difference has an effect on the momentum thickness or boundary layer momentum deficit over the entire wing. Distribution of friction coefficient over the flap is also changed in comparison with fully turbulent computation. Figure 3.24 shows the skin friction coefficient in streamwise direction (x) direction over the flap.

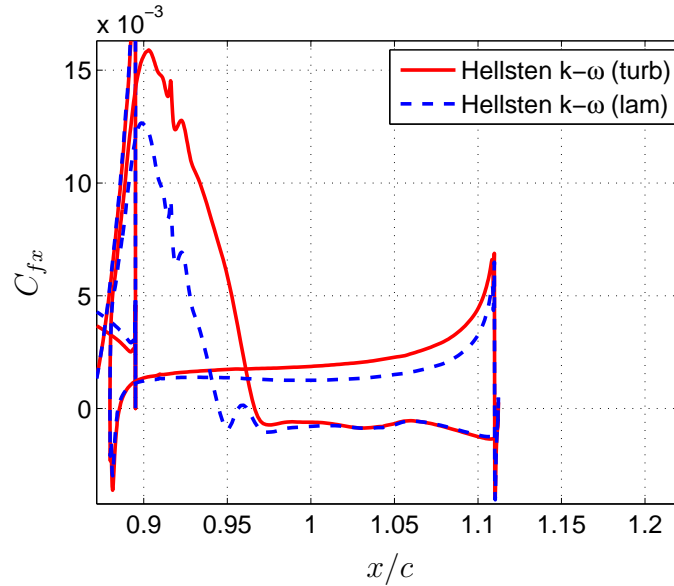


Figure 3.24: Comparison of skin friction coefficient in streamwise direction over the flap.

When the laminar area was prescribed over the leading edge of the flap from the leading edge to $x/c = 0.95$, The Hellsten $k-\omega$ model predicts the laminar separation bubble at approximately $x/c = 0.94$. At this location the flow becomes separated which resulted in the formation of laminar separation bubble. Downstream of the laminar separation bubble, flow is reattached. But the effect of the adverse pressure gradient lead to turbulent boundary layer separation arising at $x/c = 0.96$. Therefore, large separation bubble is developed in this area which affects the pressure distribution over the flap. Figure 3.25 depict the velocity streamline around the flap.

The laminar separation bubble does not exist in the fully turbulent computation, where boundary layer separation occurs at $x/c = 0.96$.

Figure 3.26 shows a comparison of the skin friction distributions predicted by the S-A model in computations with, respectively, full-turbulence assumption and prescribed local laminar region.

The same trend as we observed for resulted C_f from Hellsten $k-\omega$ model is observed here. At the leading edge of the main element, C_f is reduced considerably and the laminar boundary layer is developed to the point where $x/c = 0.2$ and after that transition to turbulent is occurred and skin friction starts to increase. After the transition point, the obtained C_f is higher than the fully turbulent calculation. However, prediction of the skin friction around the flap is changed in comparison with fully turbulent assumption.

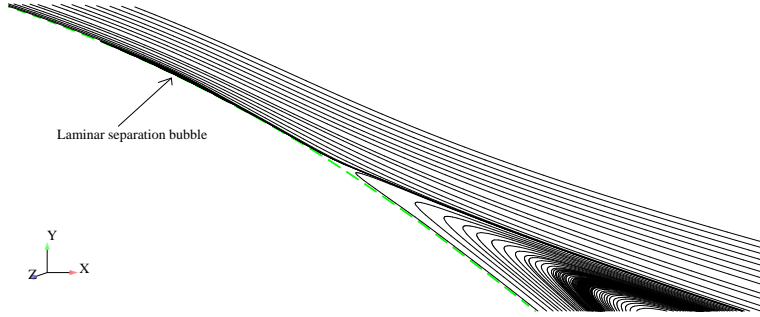


Figure 3.25: Velocity streamlines over the flap for the Hellsten $k - \omega$ model with transition calculation.

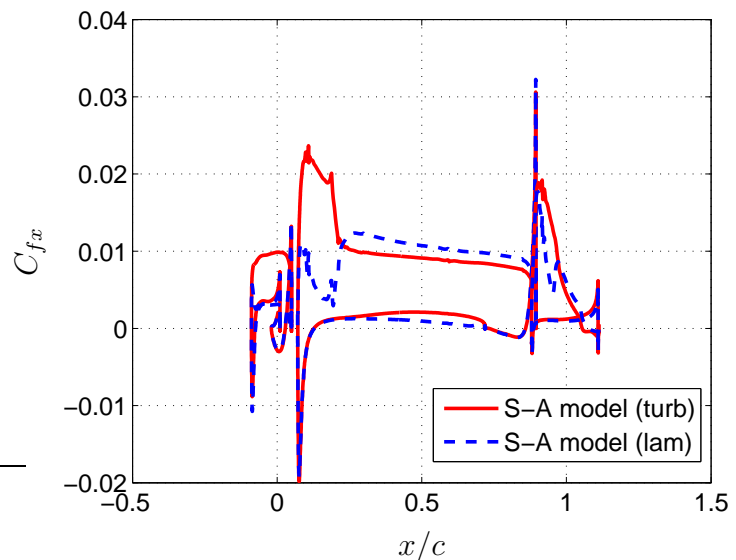


Figure 3.26: Comparison of skin friction coefficient in streamwise direction.

C_f decreases until it reaches the point $x/c = 0.95$. After that C_f starts to increase and transition occurs. S-A model did not predict the laminar separation region. However, there is a delay in the flow separation in comparison with fully turbulent computation and predicted separation location and separation length is not in accordance with experimental data. This fact has been already shown in Figure 3.19.

Figure 3.27 shows the comparison of skin friction distribution which is resulted from the Menter SST model with the assumption of fully turbulent flow and prescribed laminar area.

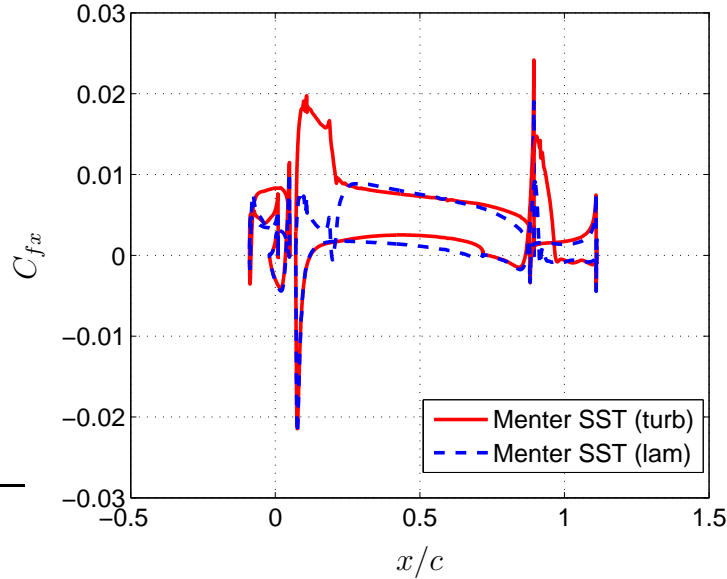


Figure 3.27: Comparison of skin friction coefficient in streamwise direction.

The skin friction coefficient is reduced over the leading edge of the main element and leads to laminar separation bubble at almost $x/c = 0.2$. However, the predicted laminar separation is very small and after the transition, the fully turbulent boundary layer developed to the trailing edge. The predicted skin friction coefficient around the flap however shows unreasonable behavior. The fall in C_f is more abrupt than the fully turbulent calculation and at $x/c = 0.91$ laminar boundary layer separation occurs and a laminar separation bubble is formed. Shortly after the transition onset at $x/c = 0.93$, turbulent boundary layer separation takes place and leading to a large separation region over the flap. The flow streamlines show that the flow is almost separated over the whole flap suction side. This separation has a great effect on the upstream flow and the over estimation of pressure coefficient can be explained by the formation of this separation bubble over the flap. Figure 3.28 shows the flow streamlines around the flap obtained with the Menter SST model.

The last turbulence model used to analyze the skin friction coefficient is the low Reynolds number model called PDH LRN $k - \omega$.

This model did not predict any laminar separation bubble. Over the wing, transition to turbulent occurs at $x/c = 0.2$ and after that predicted skin friction coefficient by transition computation is higher than the C_f predicted by fully turbulent calculation.

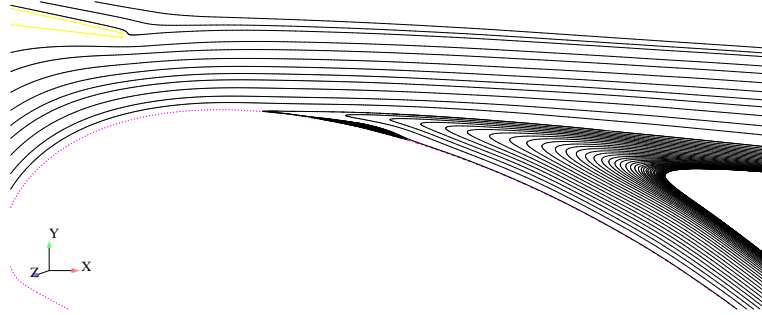


Figure 3.28: Velocity streamlines over the flap for the Menter SST model with transition calculation.

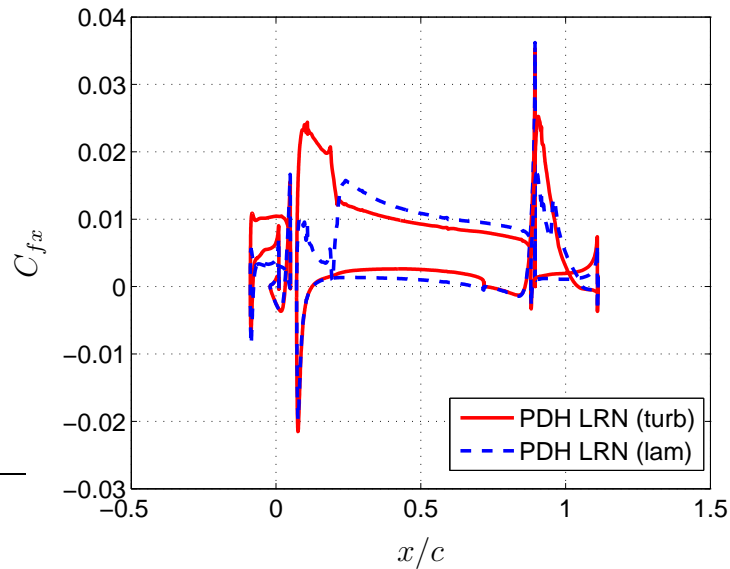


Figure 3.29: Comparison of skin friction coefficient in streamwise direction

3.4 Comparing velocity field

Velocity profiles were plotted for the main element and flap at four locations. For the main element one location was selected near the mid-chord and for the flap three locations were selected, near the leading edge, mid-chord and near the flap trailing edge. The obtained results are displayed in the figures 3.31 to 3.34.

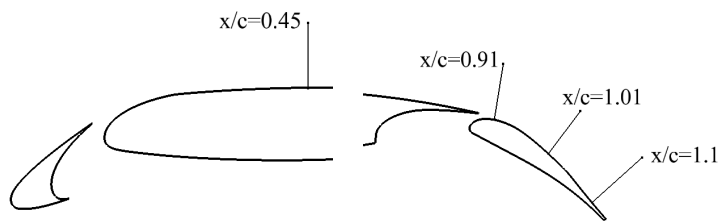


Figure 3.30: Illustration of positions where velocity profiles plotted

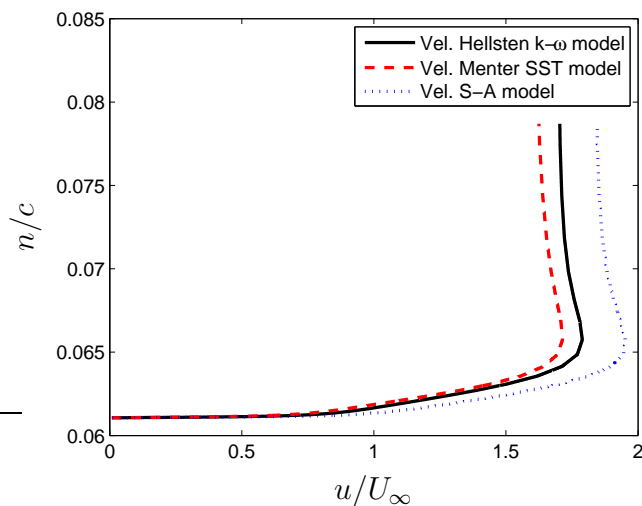


Figure 3.31: Comparison of velocity profiles on the main element $\alpha = 7.05^\circ$ $x/c = 0.45$

The slat wake passes just above the main element boundary layer and does not have a considerable effect on the velocity profile of the main element, just a little velocity deficit can be observed. The velocity predicted by the S-A model is higher than the other models.

Figure 3.32 shows the velocity profile near the leading edge of the flap. Velocity profile in this location usually consists of flap boundary layer, boundary layer due to slot effect, main element wake and slat wake. Flap boundary layer is very thin in this position. After that is the boundary layer which was formed due to the slot flow passes through the gap between the main element and the flap and formed from $n/c = 0.142$ to $n/c = 0.180$. The main element wake extend from $n/c = 0.02$ to $n/c = 0.035$ and become more symmetric. The slat wake effect does not affect the velocity profile in this location.

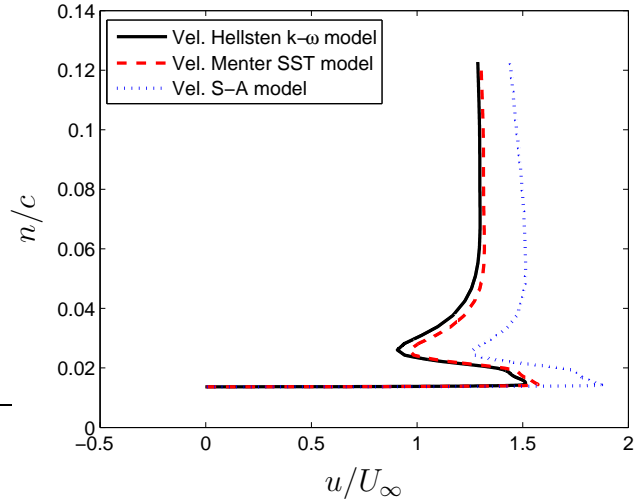


Figure 3.32: Comparison of velocity profiles on the flap $\alpha = 7.05^\circ$ $x/c = 0.92$

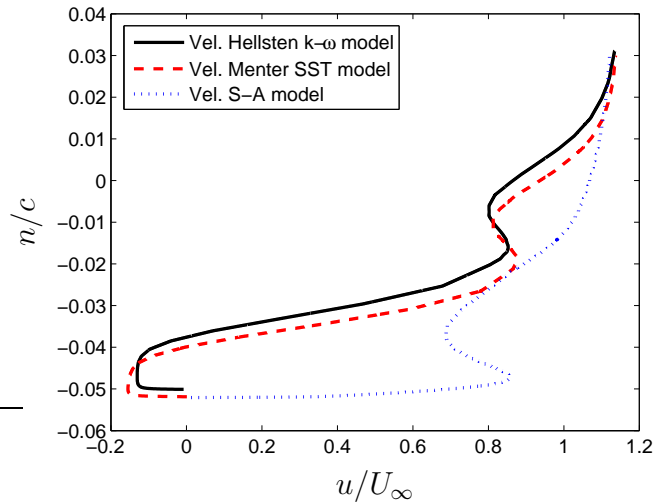


Figure 3.33: Comparison of velocity profiles on the flap $\alpha = 7.05^\circ$ $x/c = 1.02$

Figure 3.33 shows the velocity profile at the flap mid-chord. In this location the boundary layer is much thicker than at the leading edge and the main element wake seems to be merged with the flap boundary layer for the Hellsten $k - \omega$ and the Menter SST models. The Hellsten $k - \omega$ and Menter SST models have predicted reverse flow at this location due to the over-predicted flow separation. However, the S-A model shows a different performance, which does not claim flow separation at this location.

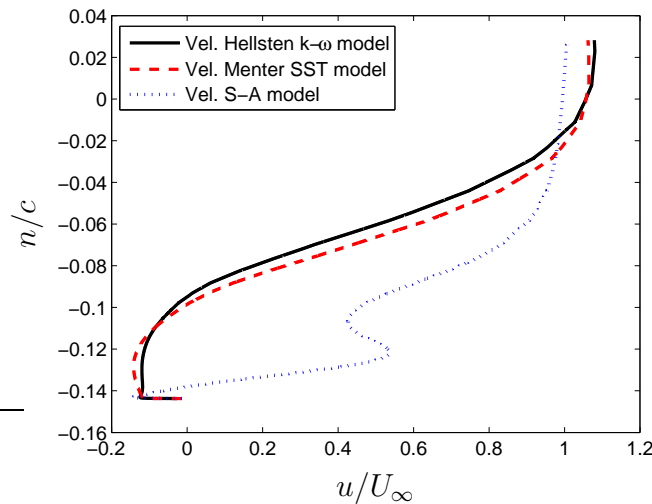


Figure 3.34: Comparison of velocity profiles on the flap $\alpha = 7.05^\circ$ $x/c = 0.10$

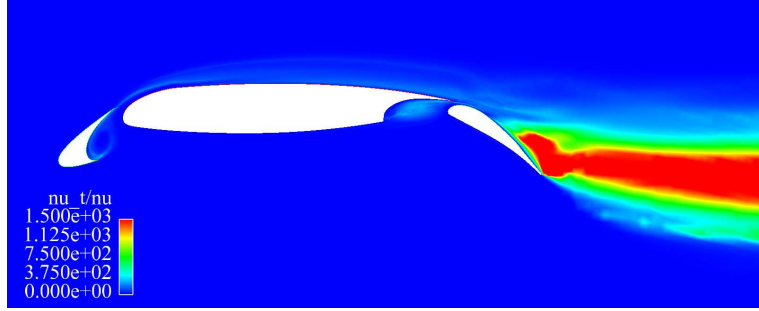
Figure 3.34 shows the velocity profile near the trailing edge of the flap. All the models predict the separation and reverse flow in this location. However, the models predicted different extension of flow separation. The separation bubble is much smaller with the S-A model in comparison with the other $k - \omega$ models.

3.5 Comparing turbulent viscosity

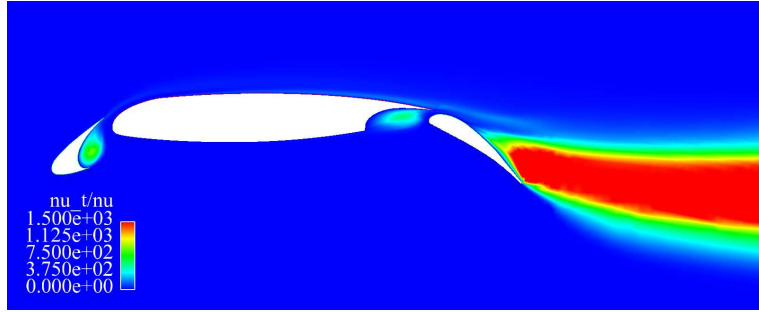
Figures 3.35a to 3.35c show the contour plot of turbulent viscosity which is normalized by the free stream viscosity ($\frac{\mu_t}{\mu}$) for Hellsten $k - \omega$, Menter SST and S-A models.

The behavior of the turbulent viscosity for the three turbulence models was investigated at four positions (the same as the velocity profiles). The obtained results for the normalized turbulent viscosity on the upper surface of the wing and the flap are shown in figures 3.36a to 3.36d.

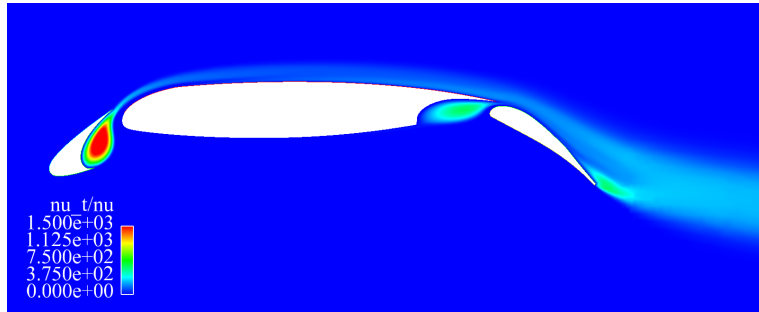
What can be seen from Figure 3.36a is that the turbulent viscosity μ_t for the Menter SST model is lower than the Hellsten $k - \omega$ and S-A models. The Menter SST model was developed in order not to over predict the shear stress in adverse pressure gradient. In adverse pressure gradient flow the production is much higher than the dissipation [15] ($P_k > \varepsilon$). In boundary layer the Boussinesq assumption can be written as:



(a) Turbulent viscosity for Hellsten $k-\omega$ model



(b) Turbulent viscosity for Menter SST model



(c) Turbulent viscosity for S-A model

Figure 3.35: contour plot of turbulent viscosity for different turbulence models

$$-\overline{uv} = C_{\mu}^{1/2} k \left(\frac{P_k}{\varepsilon} \right)^{1/2} \quad (3.2)$$

Equation 3.2 shows why shear stress over predicted in adverse pressure gradient. The SST model overcome this problem. Equation 3.3 shows the modified turbulent viscosity for the Menter SST model.

$$\mu_t = \frac{\rho a_1 k}{\max(a_1 \omega; \Omega F_2)} \quad (3.3)$$

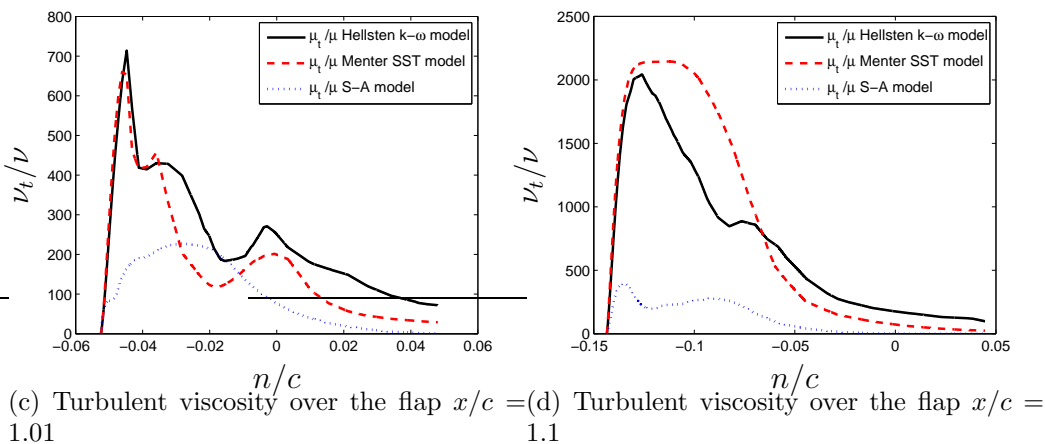
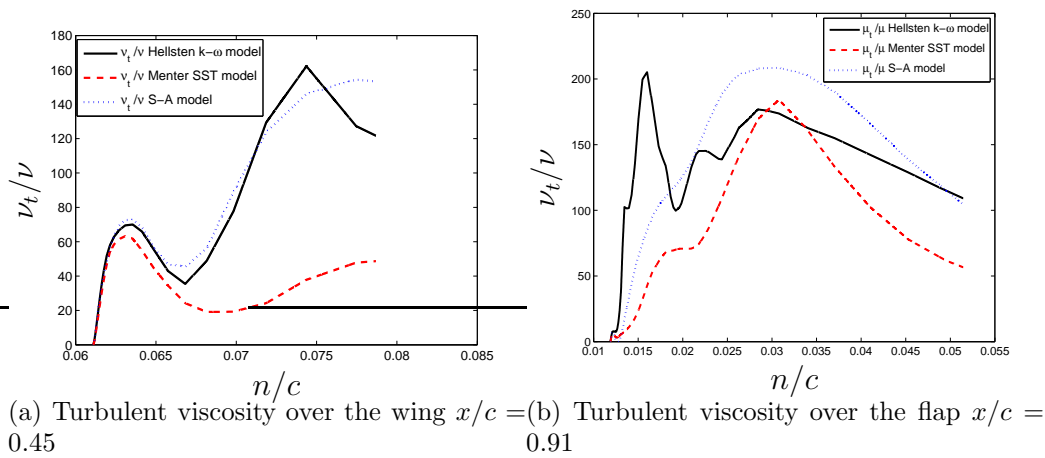


Figure 3.36: Comparison of turbulent viscosity for different turbulence models

where Ω is the vorticity (in boundary layer flow $\Omega = \frac{\partial U}{\partial y}$). F_2 is one near the wall and zero elsewhere [15].

Chapter 4

Summary and Conclusion

Four turbulence models, the Spalart-Allmaras, EARSM + Hellsten $k - \omega$, Menter SST and PDH LRN $k - \omega$ models, were applied to the high lift configuration exposed to a freestream with a Mach number of $M = 0.15$ and $Re = 2.094 \times 10^6$. The ability of these models in predicting the challenging flow-field around the three element airfoil have been examined.

The obtained results from the Spalart-Allmaras and the PDH LRN $k - \omega$ turbulence models for surface pressure distribution showed a better agreement with experimental data in comparison with the Menter SST $k - \omega$ and the Hellsten $k - \omega$ models which under predicted the suction peak over the all elements. Moreover, these models predicted different separation points and recirculation areas. The Menter SST and the Hellsten $k - \omega$ models predicted an early separation over the flap and the discrepancies with experiments is greater than Spalart-Allmaras and PDH LRN $k - \omega$ models.

A series of RANS calculations were performed in order to find out the corrected angle of attack. Angles of attack from 6° to 7.5° were examined and angle of attack equal to 6° showed best agreement with experimental data obtained for surface pressure distribution.

The turbulence models responded in different ways when transition calculation was included into the simulations. The ability of Spalart-Allmaras and the PDH LRN $k - \omega$ turbulence models in predicting the flow-field when laminar area was prescribed were better than the Menter SST $k - \omega$ and the Hellsten $k - \omega$ models. The Menter SST model predicted a big separation bubble over the flap which is not an expected result. Moreover, the Menter SST and the Hellsten $k - \omega$ models predicted the laminar separation bubbles on the upper part of the wing and flap which is not a physical phenomena and triggered a big separation bubble over the flap. Moreover, development of the boundary layer around the multi-element airfoil changed when laminar area prescribed.

Chapter 5

Future work

This thesis has been done with using of a 2D mesh and steady RANS turbulence models. Using the 3D mesh and unsteady calculations can provide more realistic results and a better understanding of turbulence structures. More advanced turbulence models like hybrid RANS-LES model and considering the local transition in calculations (specifying the laminar area) would be more in consistent with real condition and provide more precise results.

Moreover, it would be interesting to analysis the multi-element airfoil at higher angle of attacks and close to stall condition which is a challenging case for turbulence models because of the high unsteadiness of flow and massive separation which is occurred.

Bibliography

- [1] S.H. Peng. Hybrid RANS-LES modeling of turbulent flow around a three-element airfoil. In *Proceedings of 6th International Symposium on Turbulence and Shear Flow Phenomena (TSFP-6)*, Seoul, Korea, 22–24 June 2009.
- [2] A. Hellsten. New advanced $k\text{-}\omega$ turbulence model for high-lift aerodynamics. *AIAA Journal*, 43(2):1857–1868, 2005.
- [3] F.R. Menter. Two-equation eddy-viscosity turbulence models for engineering application. *AIAA Journal*, 32(8):1598–1605, 1994.
- [4] P.R. Spalart and S.R. Allmaras. A one equation turbulence model for aerodynamic flow. *La Recherche aérospatiale*, (1):5–21, 1994.
- [5] L. Davidson S.-H. Peng and S. Holmberg. A modified low-reynolds-number $k\text{-}\omega$ model for recirculating flows. *Journal of Fluid Engineering*, 119(4):867–875, 1997.
- [6] D.W. Zingg and P.Godin. A perspective on turbulence models for aerodynamic flows. *International Journal of Computational Fluid Dynamics*, 23(4):327–335, 2009.
- [7] *Edge Theoretical Formulation*, 2007.
- [8] J. Blazek. *Computational Fluid Dynamics: Principles and Applications*. Elsevier, Elsevier Ltd. The Boulevard, Langford Lane Kidlington, Oxford OX5 1GB, UK, 2005.
- [9] I. Kroo. *Applied Aerodynamics: A Digital Textbook*. Desktop Aeronautics, Inc., Stanford, CA 94309, 2007.
- [10] J. D. Anderson. *Fundamentals of Aerodynamics*. McGraw-Hill, 1221 Avenue of Americas, New York, NY 10020, 2001.

- [11] E.L. Houghton and P.W. Carpenter. *Aerodynamics for Engineering Students*. Butterworth-Heinemann, Linacre House, Jordan Hill, Oxford OX2 8DP, 2003.
- [12] F. R. Menter, R. Langtry, and S. Vlker. Transition modeling for general purpose cfd codes. *Flow, Turbulence and Combustion*, 77(1-4):277–303, 2006.
- [13] A. Krumbein. *Transition Modeling in FLOWer-Transition Prescription and Prediction*, pages 45–62. 2006.
- [14] S.H. Peng and P. Eliasson. Some modelling aspects in computations of turbulent flow around high-lift configuration. In *The 28th AIAA Applied Aerodynamics Conference*, Chicago, Illinois, 28 June - 1 July 2010. AIAA 2010-4948.
- [15] L. Davidson. Turbulence modeling. Technical report, Division of Fluid Dynamics, Department of Applied Mechanics
Chalmers University of Technology, Goteborg, Sweden, 2009.